SIMULATION OF FULL-SCALE PRESSURE RETARDED OSMOSIS PROCESSES

A Thesis

by

HUSNAIN MANZOOR

Submitted to the Office of Graduate and Professional Studies of
Texas A&M University
in partial fulfillment of the requirements for the degree of

MASTER OF SCIENCE

Chair of Committee, Ahmed Abdel-Wahab
Co-Chair of Committee, Marcelo Castier
Committee Member, Eyad Masad

Head of Department, M. Nazmul Karim

May 2019

Major Subject: Chemical Engineering

ABSTRACT

The pressure-retarded osmosis (PRO) concept can be used to generate power when solutions of different salinities are separated by a semi-permeable membrane. This work presents the development of a PRO process simulator for a bench scale and plant scale simulation. For bench scale simulation, this work takes into account the effect of internal concentration polarization (ICP), external concentration polarization (ECP) and reverse solute flux that occurs in the membrane. The bench scale model is simulated and the model is verified with experimental data. For plant scale simulation, membrane discretization (finite difference method) is employed to model concentration polarization (variation in concentration) along the membrane. This leads to the development of co and counter current process flow configurations within the simulator. For an accurate representation of a plant scale simulation, equation of state is used to determine physical properties resulting in the evaluation of accurate driving force across the membrane based on changing concentration and flowrates along the membrane. Rigorous equipment models for pumps, turbines and pressure exchangers were implemented by utilizing energy and entropy balances. The development of the simulator is done in a modular fashion such that any process configuration, may it be either single stage membrane, multi-stage membrane or a parallel configuration, can be simulated by manipulating the input files of the simulator. A Nelder-Mead based routine is adapted for the process simulator as an optimization tool. The optimizer can optimize single stage and multi-stage pressures to find the optimum power densities. All this has culminated into the development of a simulator for plant-scale PRO simulation which can reliably be used as a tool to evaluate the viability of membranes and processes.

DEDICATION

To my parents for their unconstrained love and support during my work on this project. And to that special friend who kept me sane throughout the duration of the project by constantly reminding me of the bigger picture.

ACKNOWLEDGEMENTS

I would like to thank Dr Ahmed Abdel-Wahab for accepting me into his research group and giving me the opportunity to work on this project. I would also like to thank Dr Marcelo Castier whose office door, or should I say Skype account, was always open for whenever I needed guidance during all stages of the project. I am thankful for their guidance and constructive feedback throughout the duration of my Master's research project without which its successful completion would not have been possible. I would like to thank Dr Eyad Masad for his inputs on improving the document.

I would like to especially thank Muaz Selam for his continuous support throughout this project. His initial lessons on FORTRAN programming accelerated the speed at which the simulator was developed. He was an integral part of my brainstorming process for the project, as he would guide and correct me if my ideas and concepts went off track. His in-depth understanding of thermodynamics really propelled my understanding of thermodynamics of the process and his tips on deconstructing a problem to simple elements really shaped the way I solve problems.

CONTRIBUTORS AND FUNDING SOURCES

Contributors

This work was supervised by a thesis committee consisting of Professor Ahmed Abdel-Wahab and Professor Marcelo Castier of the Chemical Engineering Program, and Professor Eyad Masad of the Mechanical Engineering Program.

The routines for the equation of state used in the development of the program were provided by Dr André Zuber. The parameter fitting routines used in the project were provided by Dr Marcelo Castier and the calculation of osmotic pressure routine was developed by Muaz Selam.

All other work conducted for the thesis was completed by the student independently.

Funding Sources

This work was made possible in part by the National Priorities Research Program (NPRP) of Qatar National Research Fund under Grant Number NPRP10-1231-160069 and in part by the ConocoPhillips Global Water Sustainability Center (GWSC).

NOMENCLATURE

A	Water permeability coefficient
A_m	Surface area of the membrane
B	Salt permeability coefficient
$C_{D,m}$	Concentration of draw solution at the membrane interface
$C_{F,m}$	Concentration of feed solution at the membrane interface
$C_{D,b}$	Concentration of draw solution in the bulk
$C_{F,b}$	Concentration of feed solution in the bulk
D	Bulk diffusion coefficient of the solute
h	Molar enthalpy
h^{ig}	Molar ideal gas enthalpy
h^{R}	Residual enthalpy
k	Mass transfer coefficient of the membrane
J_w	Water flux across the membrane
J_s	Reverse solute flux across the membrane
$\dot{n}_{p,s}$	Molar flowrate of solute permeated
$\dot{n}_{w,in}^{D}$	Molar flowrate of water entering the draw side for a given element
$\dot{n}_{w}^{J_w}$	Molar flowrate of water permeating across the membrane for a given element
$\dot{n}_{w,out}^{D}$	Molar flowrate of water exiting the draw side for a given element

$\dot{n}_i^{J_s}$	Molar flowrate of solute i permeating for a given element
P_{ref}	Absolute reference pressure
S	Structural parameter of the membrane
s	Specific entropy
$\dot{S}_{gen}$	Rate of entropy generation
s^{ig}	Ideal gas entropy
s^{R}	Residual entropy
SE	Specific energy
T_{ref}	Absolute reference temperature
$\dot{V}_p$	Volumetric rate of permeated water
$\dot{W}$	Power density
$\dot{W}_{shaft}$	Shaft power required by pump
$\dot{W}_{shaft,rev}$	Reversible shaft power

Greek letters

ε	error criterion
η_{Pump}	Efficiency of pump
$\eta_{turbine}$	Efficiency of turbine
π	Osmotic pressure of solution
ρ	Liquid density

τ	Tortuosity of the support layer
ϕ	Osmotic coefficient of solution
φ	Fugacity coefficient
Φ	Initial feed fraction flowrate h

TABLE OF CONTENTS

Page

LIST OF FIGURES

Page

LIST OF TABLES

Page

1. INTRODUCTION

Increase in global energy demands has led to large usage of non-renewable, fossil fuels. This is related to an accelerated change of the global climate due to excessive release of greenhouse gases [1]. This has raised interest in renewable energy [2] sources such as solar and wind power mainly due to reduction in the prices of these technologies recently [3, 4]. Similarly, a promising and renewable source of energy is the mixing of solutions of different salt concentrations or more commonly known as salinity gradient energy [5]. When solutions of dissimilar concentrations are mixed, the free energy of mixing is released and this energy can be captured using a hydro turbine.

Over the years, many processes have been developed to capture this energy by controlled mixing of solutions. These processes include pressure-retarded osmosis [6], reverse electrodialysis (RED) [7], capacitive mixing [8] and hydrogel swelling [9]. Among these technologies, PRO and RED have been researched quite extensively and it has been shown that PRO can have higher energy efficiency and power density than RED [10].

In brief, a PRO process utilizes a semipermeable membrane between a low salt concentration and high salt concentration solutions. Due to osmosis, water molecules pass through the membrane from the low concentration solution to the high concentration solution. However, because the expanding volume of the high concentration solution is restricted, it causes a hydraulic pressure build up which, when passed through a hydroturbine generates electricity.

The aim of this work is to develop a modular, FORTRAN-based simulator that incorporates thermodynamic properties using equation of state (EoS), mass transfer models, and

process equipment characteristics to simulate a full scale PRO process with any given process configuration and conditions.

A simulator of this nature is important due to lack of existing mathematical models with rigorous implementation of an equation of state. Moreover, a simulator that can take into account membrane inefficiencies, different flow configurations, and has the ability to simulate both bench scale and full scale membrane units and various flowsheet designs is warranted. Also, it is important to make the simulator universal in-terms of its usability to first verify the membrane performance using the experimental data at bench scale and then extend the predictions to a full scale system and analyze feasibility of various process designs using the tested membrane.

The thesis is organized by first discussing the concept of an osmotic process, followed by a review of the existing body of work in PRO. Then the underlying models used in the development of various equipment and their implementation is discussed in the Methodology chapter. Then the results were presented and discussed and followed by concluding remarks of the work undertaken for this thesis.

2. LITERATURE REVIEW

In this section the discussion is initiated by describing the osmotic process, followed by demonstrating the process design of a typical PRO process and then reviewing body of work available in the literature on PRO.

2.1. Osmotic process

Osmosis occurs when there exists gradient in chemical potentials between solutions separated by a semipermeable membrane [11]. When, for example, seawater is placed in a system separated by a membrane with pure (fresh) water, water transfers from a high chemical potential region (fresh water) to a low chemical potential region (seawater) as it is illustrated by Figure 1.

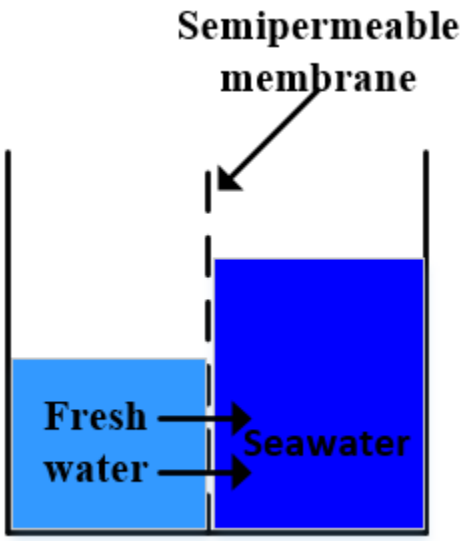

Figure 1: Principle of osmosis. Figure adapted from [12]

Three types of osmotic flows can occur, depending on operational conditions when two solutions of varying salinities are in contact via a semipermeable membrane. They are forward osmosis (FO), pressure retarded osmosis (PRO) and reverse osmosis (RO) [13]. Figure 2 shows the different types of osmotic processes when pure (fresh) water and saline water are in contact.

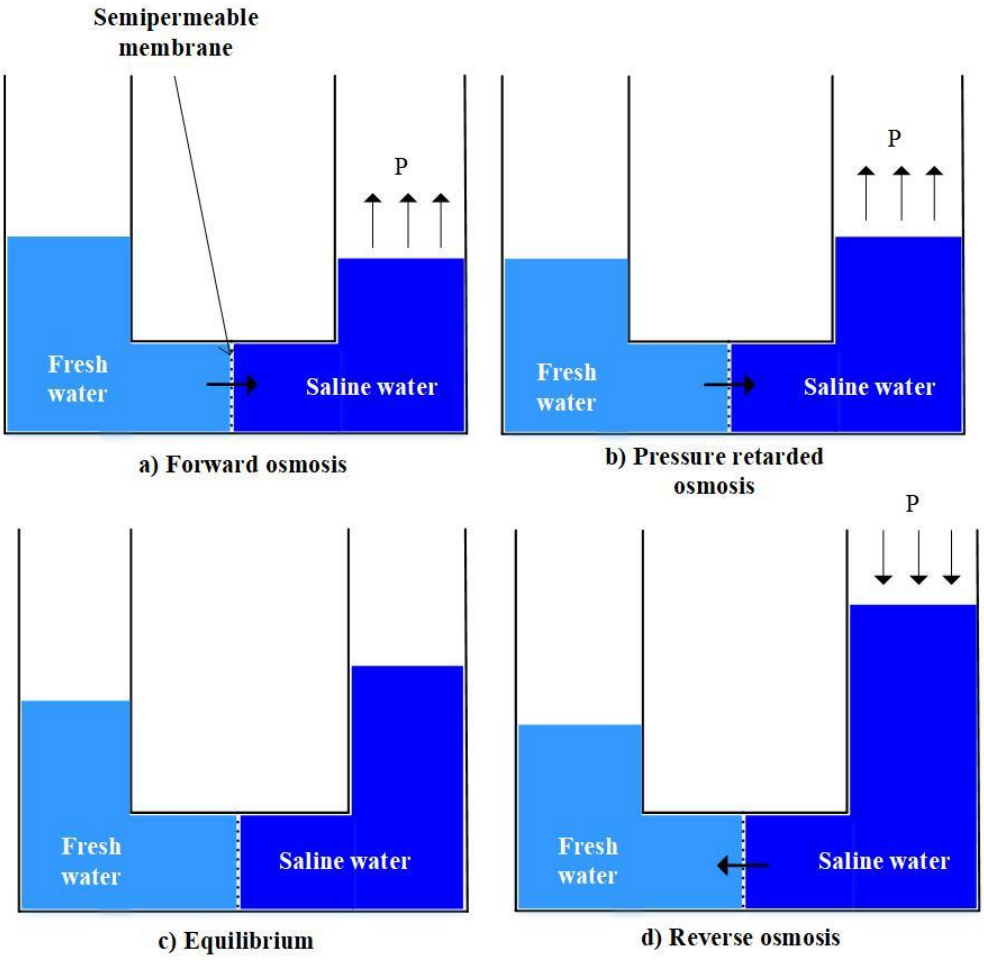

Figure 2: Various osmotic processes. Figure adapted from [14]

Forward osmosis occurs when the water passes from pure water side to saline water side. This phenomenon occurs due to the difference between the chemical potential of pure water and

of water in the saline solution giving rise to a gradient that favor the passage of water. This can also be explained by considering the osmotic pressure and the hydraulic pressure of the solution on either side. Due to salinity difference, the difference in osmotic pressure, $\Delta\pi$, is higher than the difference of hydrostatic pressure of the solution on either side, ΔP, as in Figure 2a.

As pure water moves across the membrane, it dilutes the saline solution, whose level begins to rise in the column, increasing the hydrostatic pressure on saline solution side. This leads to a condition where $0 < \Delta P < \Delta\pi$. This is called pressure retarded osmosis because the flux of water across the membrane is retarded due to increase in the pressure on the saline solution side as demonstrated by Figure 2b. Water will continue to move across the membrane as long as the difference in osmotic pressure is higher than the difference in hydrostatic pressure between the two solutions. An osmotic equilibrium is achieved when there is no net water flow across the membrane (Figure 2c). At this condition, the chemical potential of water is the same on both sides of the membrane and $\Delta P = \Delta\pi$.

Increasing the hydrostatic pressure on the saline water solution side such that $\Delta P > \Delta\pi$, causes water to flow from saline solution to the pure water side. This phenomenon is known as reverse osmosis (Figure 2d), in which the chemical potential of water in the saline solution side is higher than in the pure water side.

The osmotic phenomenon of pressure retarded osmosis described above can be used to harness osmotic energy. For a steady power production, the saline solution side is maintained at constant pressure while the pure water side provides a constant flow through the membrane, increasing the volume flow on the saline solution side, which is at a relatively high hydrostatic pressure. Then, the high pressure saline solution is passed through a hydroturbine to generate power.

2.2. Typical PRO process

A PRO process configuration for a PRO operation is shown in Figure 3. The design represented by the schematic is assumed to be the most efficient design for a single stage (single membrane module) operation. Here, the draw (high concentration of solutes) stream passes through a pressure exchanger (PX) where some of the energy from the membrane output is recovered. The partially pressurized draw stream is then fed into a booster pump to increase the pressure of the draw stream to the required operating pressure of the membrane. It is then passed through the membrane, where it gets diluted by the feed (less concentration of solutes) stream. To recover pressure work and to minimize the pumping requirement of the booster pump, the pressurized diluted draw stream is split and part of it sent to the pressure exchanger to transfer energy to the fresh draw solution. The rest of the diluted stream is sent to the hydroturbine, where energy is recovered due to increase in volume at constant pressure in the draw solution side of the membranes.

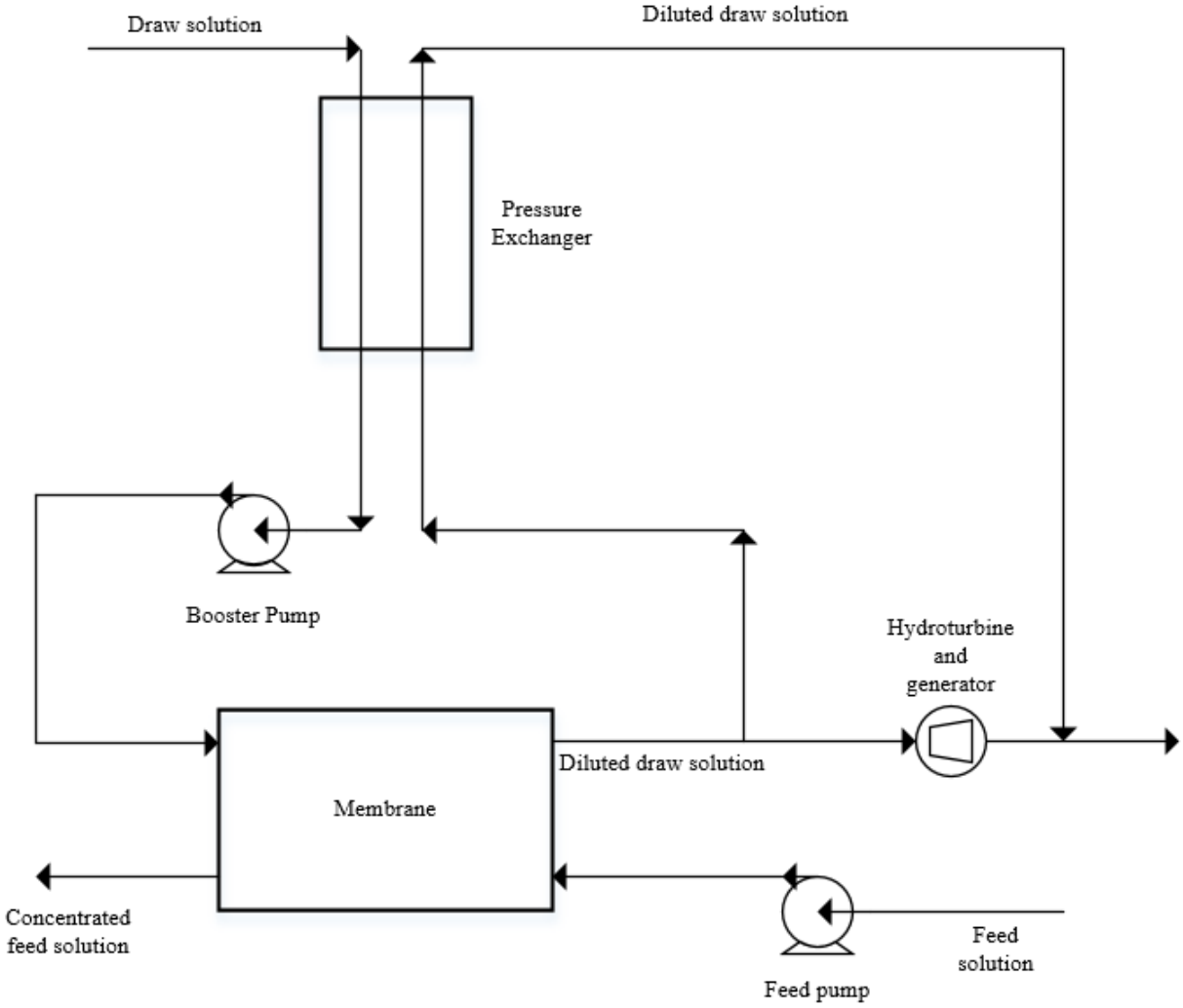

Figure 3: PRO schematic diagram. Figure adapted from [15]

2.3. Development of PRO

The idea of utilizing salinity gradients to recover energy was first reported by Pattle [16]. But research in this area was not given much attention at the time due to availability of affordable fossil fuel. In the mid-1970s, the world's energy crisis provoked further research into PRO and it significantly gained attention when Loeb et al. [6] and Loeb [17] published their theoretical and experimental results showing the feasibility of PRO. Mehta and Loeb [18], [19]

along with Lee et al. [20] investigated the various phenomena that occurred in the membrane and found that internal and external concentration polarization severely hindered the performance of the membrane.

Based on the results of Lee et al. [20] , Loeb et al. [21] conducted several experiments to determine the theoretical mechanical efficiency of the process and concluded that counter-current PRO configuration show higher efficiencies relative to co-current flow configurations. Lee et al. [20] showed that, for an ideal membrane, with perfect mixing and no concentration polarization, the water flux (J_w), as a function of water permeability of the membrane (A), osmotic pressure difference ($\Delta\pi$) and hydrostatic pressure difference (ΔP), is given by:

$$J_w = A\left(\Delta\pi - \Delta P\right) \tag{1}$$

The maximum power density, that is, the power output per unit area of membrane utilized, can be achieved by operating the process at a hydrostatic pressure difference that is half of the osmotic pressure difference across the membrane. This is strictly true for dilute solutions and ideal membrane.

In the mid-2000s, findings published by Skilhagen et al. [22], Gerstandt et al. [23] and Thorsen and Holt [24] encouraged Statkraft to open the world's first PRO power plant prototype in 2009 in Norway. This plant primarily operated on seawater and river water pairing. The plant halted its operation due to insufficient power production. Statkraft reported that reverse salt fluxes, membrane fouling, and concentration polarization were the main reasons for the unfeasible power production [13]. It was concluded that significant improvements in membrane technology must be made before PRO processes can be economically feasible.

Straub et al. [25] conducted a comprehensive review of power generation from salinity gradients, especially from seawater and river water pairing. They concluded that even though the theoretical total amount of extractable energy from a river water and seawater pairing is vast, the density of this energy is low, equal to 0.256 kWh per cubic meter of initial river water and seawater volume [26]. Thus, any extra energetic input (e.g., pre-treatment, pumping) into a PRO process can drastically reduce the efficiency of energy conversion. They also stated that alternative solution pairings that utilize hypersaline waters as draw solution must be further studied to determine the practicality of these unconventional sources and the relevant process designs.

Bajraktari et al. [27] review on using hypersaline solutions for PRO showed that experimental power densities increased by factors of 2.5 - 3.75 [28-30] when using draw solutions with salinities between 1.0 to 2.0 mol/L. This was achieved when operating at relatively low operating pressure (<20 bar) and can be even higher when operating at higher pressures since the optimum for hypersaline solutions is higher. It was also shown that when using hypersaline solutions schemes, the theoretical extractable energy density approached and exceeded 1kWh per cubic meter of mixed solutions [31] which is significantly higher than that for a seawater and river water pairing. Their review also stated that increasing the operating pressure for a PRO process leads to deformation of the membrane [28, 30, 32, 33], which is a serious limitation to operating a PRO process using hypersaline solutions. In addition, these studies showed that, where water permeability stayed constant (no damage to the membrane), the salt permeability increased with increase in applied hydraulic pressure. This increase in salt permeability causes the performance of the membrane to be lower than the theoretical predictions where the salt permeability is assumed constant. Bajraktari et al. concluded that more

work needs to be done on the system design for hypersaline solution schemes, such as adopting multi-stage design for lowering the operating pressures, and developing membranes with high mechanical strength that can operate at higher pressures.

Over the years, numerous mathematical mass transfer models have been developed to predict the performance of a lab scale membrane operating in PRO mode. One of the first contribution to this area was made by Loeb [17] who assumed the existence of a porous substructure acting as boundary layer. This model was then modified by Lee et al. [20] taking into account the effects of internal concentration polarization. Although the model is able to predict the membrane performance with reasonable accuracy, it is noted that additional performance limiting phenomena, such as external concentration polarization, were still not taken into account in the development of this model. Achilli et al. [34] further developed the model by taking into account dilutive external concentration polarization at the active membrane layer side but ignoring the reverse salt permeation and other performance limiting phenomena in their development. Yip et al. [35] further enhanced the development of the mass transfer model by incorporating internal concentration polarization (ICP), external concentration polarization (ECP) and reverse salt permeation (RSP). They verified their model with experimental results they generated for various membranes with different properties and it has shown to give reasonable agreement.

Naguib et al. [36] developed two mathematical model to simulate PRO membrane unit. One model is used to predict the bench scale performance of a membrane while the second model is used to predict the performance of commercial length membranes. They utilized the ideal van't Hoff equation for prediction of osmotic pressures and the mass transfer model developed by Yip et al. [35] along with modifications to the mass transfer model to account for

concentrative external polarization. They showed that the performance of full scale membranes, when compared to bench scale membranes is significantly reduced due to variation in concentration difference and volumetric flowrates of permeate along the length of the membrane. They concluded that these variations can be minimized by adjusting various conditions such as flowrates and membrane properties. They also showed that high flux membranes at bench scale will not necessarily perform significantly better when compared to low flux membranes at full scale. This is mainly due to severe dilution at full scale for a high flux membrane, which can equalize the membrane performance of both the high flux and low flux membrane. Hence, they concluded that further studies must be performed to minimize axial variations and to determine optimum conditions for high power densities.

Maisonneuve et al. [37] built upon the conclusions and the mathematical modeling of Naguib et al. by incorporating pump, turbines and pressure exchangers into their model. They also incorporated pressure drop along the membrane that is dependent upon the fluid velocities, densities and membrane channel diameter. Using co-current flow as their process configuration and process conditions adopted from Achilli et al. [34] in their experiments, they set out to determine the optimum inlet draw and feed velocities along with operating pressure that would result in the maximum power density for a full-scale and bench scale membranes. In their analyses, they showed that, when using full-scale optimized parameters for feed and draw velocities and operating pressures, they were able to achieve optimum power density of 7 times higher than when compared to using optimized parameters from bench scale simulation. This clearly shows that the optimum parameters at the bench scale simulation are not directly transferable to full-scale simulation due to various non-linear effects caused by dilution of the draw stream and concentration of the feed stream.

He et al. [38] realized the complexity of solving the highly non-linear mass transfer equation for a full scale PRO membrane and hence, applied a first order Taylor series expansion to the water flux equation developed by Yip et al. [35] along with simplification of van't Hoff approximation for the prediction of osmotic pressures of the streams. They validated their approximation with experimentally published data for bench scale membranes and concluded that their approximation for water flux prediction works best with membranes that have low water permeability.

Straub et al. [39] carried out full scale PRO analyses using the van't Hoff equation for osmotic pressure predictions and mass transfer model developed by Yip et al. [35] to assess the performance of co-current and counter-current flow configurations along with optimization of applied hydraulic pressures, initial feed flow fractions, $\Phi = \dot{V}_{F,0} / \left(\dot{V}_{F,0} + \dot{V}_{D,0} \right)$ where $\dot{V}_{F,0}$ and $\dot{V}_{D,0}$ are the initial volumetric flowrate of feed and draw streams, respectively, and membrane area. They used seawater (0.6M NaCl) and river water (0.015M NaCl) as draw and feed solution respectively, as the osmotic pressures for these solutions can be predicted by van't Hoff equation with reasonable accuracy. In their analyses, they showed that counter-current flow recovered higher energy and higher power densities when compared to co-current flow. This was mainly attributed to the fact that, in counter-current flow, the entire membrane area is utilized for energy production because the driving force along the membrane being relatively constant. This is inherently due to the flow direction of the feed solution being opposite to the draw solution. Conversely, in a co-current flow, the driving force is higher at the start of the membrane but, as the water is permeated into the draw solution, rapid drop in osmotic pressures causes the driving force to rapidly diminish, leading to lower energy recovery. They also concluded that every PRO

process design would have its own set of optimized parameters such as applied hydraulic pressures, initial feed flow fractions, and membrane area, but an initial feed fraction flowrate of 0.5, and hydraulic pressures of $\Delta P = \Delta\pi / 2$ are good initial estimates for the optimization routines.

Altaee et al. [40] proposed a dual stage PRO process where the draw solution (seawater) is treated in one stage and part of it, equal to the membrane permeate flowrate, is split and sent to the next stage for further extraction of osmotic energy, as shown in Figure 4. Each stage utilized feed solutions of different salinities (0.2 g/L for wastewater and 1 g/L for brackish water). The aim of their work was to study the advantages of a two-stage PRO process by continuously treating the draw stream in two stages whilst using fresh feed solution for each stage. This was done so that the effect of fouling on membranes caused by using wastewater as feed could be reduced by using lower amounts of wastewater in conjunction with brackish water and determine configurations that would lead to net higher energy recovery. They varied salinities of brackish water from 1 g/L to 5 g/L at each stage to check for optimum performance of the given configuration. They concluded that use of brackish water and wastewater as feed for first stage and second stage, respectively, performed better than all the other configurations that they evaluated. They showed that the second stage pressure for optimum power density was lower than $\Delta\pi / 2$ because of the dilution of the draw stream from the first stage. They also concluded that their dual stage PRO process utilized higher membrane area than a conventional PRO process, which resulted in a net higher energy recovery.

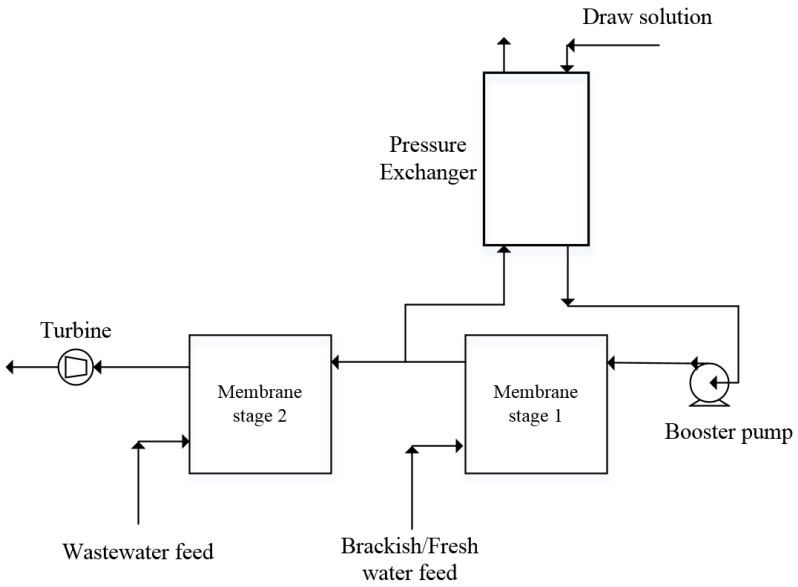

Figure 4: Proposed dual stage PRO design by Altaee et al. Figure adapted from [40]

Altaee and Hilal [41] modified the design configuration shown in Figure 4 by eliminating the split of the draw solution after the first stage and allowing the entire draw solution to be fed to the second membrane and then introducing the split such that the permeate flowrate from the membrane is passed through the turbine and the rest is send back to the pressure exchanger, as presented in Figure 5. They also varied the draw solution salinity from 35 g/L to 40 g/L and used a salinity of 0.2 g/L for their brackish water feed solution. They showed that the cost of the membrane reduced by using 40 g/L draw solution and brackish water as feed solution for each stage. This was attributed to higher osmotic pressure difference between the solutions, hence requiring lesser area for the overall two stage membrane unit. They also showed that the power density of their new proposed configuration increased by 17.4% using 45 g/L seawater as draw solution when compared to the configuration given in Figure 4. Although these results look promising, no comparison was done against a single stage PRO process with the same area. Moreover, a simplified mass transfer model and the van't Hoff equation were used to predict the

water flux and the osmotic pressure of solutions, which are good for qualitative analysis but do not give a clear picture when numerous mass transfer limiting effects are present and non-linearity of osmotic pressure caused by the concentration of the solutions needs to be considered.

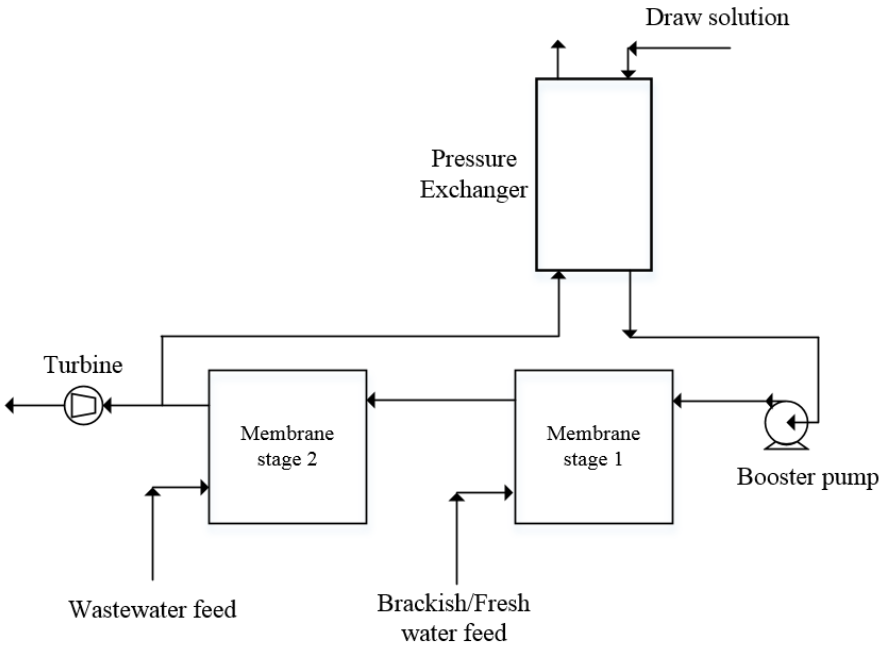

Figure 5: Modified design by Altaee and Hilal. Figure adapted from [41]

He et al. [42] carried out energy and membrane performance analysis on two stage co-current flow schemes. They analyzed four different configurations as follows:

- Continuous draw and continuous feed (CDCF) where both the draw and feed streams are continuously fed in the first stage and second stage as shown in Figure 6a.
- Divided draw and divided feed solution (DDDF) where part of draw and feed streams are split before entering the first stage and fed to the second stage, effectively making it 2 single stage PRO process with lower flowrates to each stage, as shown in Figure 6b.

- Continuous draw and divided feed (CDDF) where the draw stream is continuously treated in 2 stages whereas the feed stream is split before entering the first stage and is fed to the second stage as fresh feed, as shown in Figure 6c
- Divided draw and continuous feed solution (DDCF) where the draw is split before entering the first stage and fed to the second stage as fresh draw stream but the feed stream is continuously fed from the first stage to the next, as shown in Figure 6d.

In their analyses they showed that, for a limited area full-scale simulation where the osmotic equilibrium is not reached between the draw and feed solution, CDCF and CDDF configurations tend to give higher net power densities, power density of a two stage minus power density of one stage PRO process, when compared to DDDF and DDCF configurations. They also showed that for higher membrane areas and at higher initial feed flowrate fraction, the relative average power density, net power density over power density of one stage PRO process, for CDCF is higher compared to CDDF configurations. They concluded that for CDCF and CDDF configurations the distribution of area for the first and the second stage and the initial feed flowrate fraction played an important role in determining the optima for power density calculations. Moreover, they also concluded that at higher initial feed fraction flowrates the optimum hydraulic pressure are lower for a PRO membrane compared to when operating it at lower initial feed fraction flowrates. This could potentially mean that at higher salinities, optimum for membranes could be potentially lowered by operating the process at high initial feed fraction flowrates.

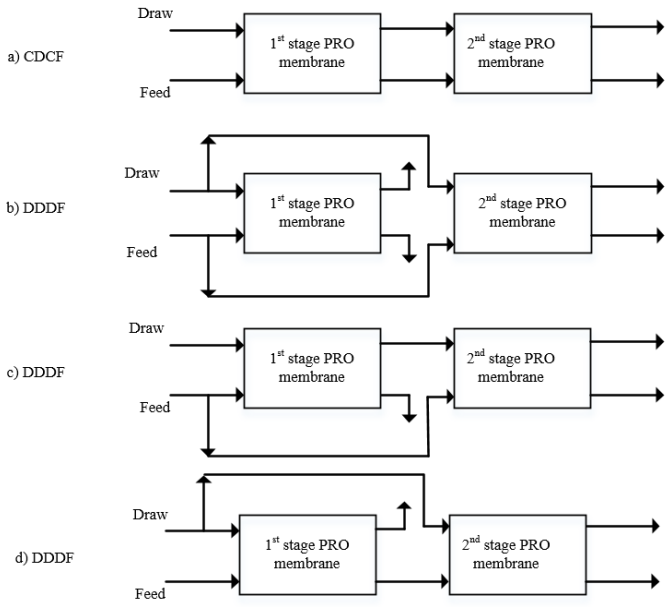

Figure 6: PRO process configuration investigated by He et al. Figure adapted from [42]

Altaee et al. [43] evaluated the potential and energy efficiency of a dual stage PRO process by using a PRO process design they proposed in their earlier work [40] (Figure 4). They conducted a numerical study on various draw and feed solution combinations that included Dead Sea water (5 M NaCl), reverse osmosis brine (1.2 M NaCl), seawater (0.6 M NaCl) and wastewater (0.017 M NaCl) solutions. They compared the energy efficiency of having a PRO setup with larger area or splitting the areas into two stages, respectively based on their proposed design. They showed that for Dead Sea-seawater and dead sea-RO brine combination, their proposed design (Figure 4) harvested more energy compared to using larger area in one stage. This was mainly due to concentration polarization on the feed side. As the feed solution is already concentrated (seawater or RO brine), the overall water flux across the membrane in a single stage with large area is lower due to internal concentration polarization. As the feed gets more concentrated along the membrane, the internal concentration polarization becomes

significant on the feed side further hindering the water flux. Hence, when a fresh feed is fed to the second stage the osmotic pressure difference is rejuvenated and concentration polarization is mitigated. Therefore, more salinity gradient energy can be harvested from the given draw solution by continuously treating the draw stream in the first stage and second stage. But for combinations of Seawater-wastewater, Dead Sea-wastewater and RO brine-wastewater, there was no improvement in using the proposed dual stage PRO for harvesting the salinity gradient energy. Since the feed solution concentration is relatively low, the internal concentration polarization effect does not dominate significantly along the membrane as the feed solution gets concentrated when compared to feed solutions made of RO brine or Seawater. Therefore, adding a second stage and using fresh feed solution does not improve the osmotic pressure difference hence not improving the saline gradient energy recovery. They concluded that adding fresh feed to the second stage remains a key parameter that significantly improved the process performance in terms of harvesting salinity gradient energy.

In an attempt to achieve higher thermodynamic efficiency, Bharadwaj et al. [44] conducted a numerical study on a multi-stage PRO systems. They carried out their analyses on an idealized seawater-river water pairing, where the osmotic pressures of the solutions were given by the van't Hoff equation. To simplify their calculations, Bharadwaj et al. defined an overall effectiveness of the membrane based on fluxes reaching equilibrium. This definition inherently accounted for mass transfer behavior and dilution effects, effectively treating the membrane as a black box with no pressure drop and no rigorous analysis of the polarization effects within the membrane. The inflows to the membrane were in co-current configuration, and they utilized isentropic efficiencies for pumps and turbines. They found that different intermediate optimum stage pressures exist that result in different optima for work based on the

target functions specified. They concluded that utilizing a more rigorous mass transfer model and counter-current flow designs will offer more in-depth understanding of process design.

Moreover, module scale or full scale analysis conducted on PRO process has shown that the optimal operating conditions such as applied hydraulic pressure equal to half the osmotic pressure difference for maximum power recovery and equal amounts of feed and draw solutions are good initial estimates for calculations of optimal power but the real optima for a full scale design differs due to the numerous non-linear effects within the membrane. This includes concentration polarization of the membrane at the feed solution side and dilution of the draw streams that leads to change in driving force along the membrane [45, 46]. These studies are mostly conducted using generic correlations to estimate the fluid properties and do not truly take into account the non-linearity of the process. Hence, for a rigorous analyses of a full scale system with various process designs, an appropriate thermodynamic package is necessary to evaluate stream properties, real work done by pumps, turbines and pressure exchangers to determine optimal process conditions and process designs.

These computational studies, while exploring the full breadth of PRO process configurations, are generally based on idealistic assumptions of equipment performance and fluid property behavior. Such studies, while useful in underscoring qualitative trends in process behavior, have shortcomings when applied to the generation of quantitative data relevant to the design and evaluation of real, full-scale units. The absence of realistic models for electrolyte thermodynamics and irreversible effects in any formulation casts doubt on its ability to inform decisions on process feasibility. Moreover, most of the previous studies are primarily aimed at seawater and river water pairing and there exists gaps in literature on in-depth studies of

alternative solution pairing such as hypersaline water from the Dead sea or water produced from extraction of oil from oil fields, with seawater.

This research aims to make the following contributions:

- Incorporation of an equation of state (EoS) that can determine electrolyte solution properties accurately for a PRO process, along with detailed models for membrane, pumps, turbines and pressure exchanger units for the purpose of process design.
- Interface a suitable optimizer program with the developed simulator to carry out optimizations for various proposed process configurations;
- Analyze a multi-stage PRO process where the hypothesis is that each stage would have a different optima due to continuous dilution.

2.4. Thermodynamic package for electrolyte solutions

The development of the simulator necessitates that an appropriate thermodynamic model be chosen so that properties such as Gibbs free energy, osmotic pressure, liquid densities, enthalpies and entropies are accurately determined. This helps in ensuring that parameters such as power density (energy output per unit area of membrane) or specific energy (energy output per total volume of inlet streams to the membrane) or net energy (energy input by the pump minus energy output by the turbine) used in evaluating the performance of a PRO process are determined properly and can be used to make design predictions. Since the process primarily deals with electrolyte solutions, it is natural to look into equations of state that are developed to predict their properties. Table 1 shows some of the EoS available in the literature that are specifically developed to model electrolyte solutions and are based on expressions for the Helmholtz free energy. These EoS are developed by treating the contributions of short-range

(dispersive) and long-range (electrostatic) interactions to the Helmholtz free energy of the system as additive. This leads to the development of theories to model each of these contributions [47].

Table 1: Existing Models for electrolyte solutions. Adapted from [48]

Model Description	Reference
Peng-Robinson + Born term + MSA	[49]
PC-SAFT + Debye-Hückel (ePC-SAFT)	[50]
Mattedi – Tavares-Castier (MTC) + Born term + MSA (Electrolattice/Q-electrolattice)	[51, 52]
SAFT-VR Mie + Born term + Debye-Hückel (eSAFT – VR Mie)	[53]
Soave-Redlich-Kwong + TPT1 Association + Born term + Debye-Hückel (e-CPA)	[54]
SAFT-VR Mie + Born term + MSA (SAFT-VR Mie)	[55]

There also exists models in the literature that are based on excess Gibbs energy and are commonly known as activity coefficient models. These models are very common alternatives to Helmholtz free energy models such as those listed in Table 1. They allow the evaluation of phase equilibrium conditions and calorimetric properties of electrolyte solutions but they do not provide any volumetric properties. A few examples of activity coefficient models are the Pitzer

[56, 57] and the NRTL-SAC (Nonrandom Two-Liquid Segment Activity Coefficient) model extended to electrolytes [58].

The Q-electrolattice and eSAFT-VR-Mie EoS have shown very good performance in the correlation and prediction of electrolyte solution properties [52, 53], and their computational implementations were readily available at Texas A&M University at Qatar. Hence, a brief background of their formulation is given below and a parameter optimization strategy is elaborated for comparison between the two EoS in the methodology chapter.

2.4.1. Q-electrolattice equation of state

The development of this EoS follows the same methodology as presented by Myers et al. [49], which takes into account the development of the electrolyte EoS based on Helmholtz energy approach. The thermodynamic path considered in the development of this model is presented by Zuber et al. [51]. The residual Helmholtz energy path mentioned by Zuber et al. for the model is given by:

$$A^R\left(T,V,n\right)=\Delta A^{MTC}+\Delta A^{Born}+\Delta A^{MSA} \tag{2}$$

where, ΔA^{MTC} is contribution to the Helmholtz energy for short range interactions, including short range ion-ion interaction. This term was developed based on the generalized van der Walls and lattice fluid theory and the details of the development of this term can be found in [59]. ΔA^{Born} is the contribution to the Helmholtz energy due to solvation effects (interaction between the ions and the solvent) and the equation describing the said interaction can be found in [52]. The term ΔA^{MSA} is the contribution to the Helmholtz energy due to long range ion-ion interactions.

2.4.2. eSAFT-VR Mie equation of state

In the development of eSAFT-VR Mie equation of state, the residual Helmholtz free energy is given by:

$$A^{res} = A_{seg} + A_{chain} + A_{assoc} + A_{DH} + A_{Born} \quad (3)$$

where, $A_{seg}, A_{Chain}, A_{assoc}$ are segment, chain and association terms that describe the non-electrolyte part of the solution and the development of these terms follow the same formulation of Lafitte et al. [60]. A_{DH} is the contribution to the Helmholtz energy due to long range ion-ion interactions provided by the Debye-Hückel theory. The term A_{Born} is the contribution to the Helmholtz energy due to solvation effects. Equations for the above described terms can be found in [53].

3. METHODOLOGY

In order to achieve the objectives of this research, it is necessary to develop a simulator that is flexible and can carry out multiple configurational analyses based on the desired process design and conditions. The tasks outlined below are necessary to achieve the research goals:

- Selection of the thermodynamic model and its parameters;
- Implementation of the membrane, pump, pressure exchanger and turbine modules;
- Development of computational code to allow the simulation of different process configurations through changes of equipment connectivity;
- Development of counter/co-current schematic for PRO operation;
- Validation of the simulator results using published experimental data.

3.1. Re-optimizing of thermodynamic package

A parameter optimization strategy similar to the one adopted by Zuber et al. [52] for Q-electrolattice EoS is followed. However, instead of optimizing the EoS parameters against experimental mean ionic activity coefficients and liquid densities, they are optimized against osmotic coefficients and liquid densities. This was done in order to achieve accurate and better predictions for the osmotic coefficient, which closely related to the osmotic pressures of the streams. The accurate evaluation of osmotic pressure differences is very important because, as indicated by Equation (1), the flow rates across the membrane is driven by it.

To ensure that the thermodynamic model can reliably predict the properties of draw and feed solutions that might have various ions (salts disassociate into ions when dissolved in solvent), different feed sources are analyzed such as the hypersaline produced water from oil platforms, seawater and reverse osmosis brine to identify the different ions that might be present

in the solutions. Table 2 shows the various major ions that potentially might exist in the feed sources described.

Table 2: Ions present in various draw and feed solutions

Ion	Charge
Sodium (Na)	1^+
Potassium (K)	1^+
Magnesium (Mg)	1^+
Calcium (Ca)	2^+
Chloride (Cl)	1^-
Sulphate (SO_4)	2^-

To reduce the computational time and load on refitting the parameters, a strategy similar to that of Held et al. [50] is applied where the aqueous solution is divided into subgroups of various ions based on their similarities, as presented in Table 3. Parameter fitting is then carried out in a manner where, for example, group 1 ion parameters are simultaneously fitted for all three ions. Then, for group 2 only parameters for Mg^{2+} are fitted while retaining the Cl^- ion parameter values that are obtained from group 1. In a similar fashion the SO_4^{2-} ion parameters are fitted by retaining the values of other positive ion parameters that were obtained in the previous optimization step. Since the parameters are optimized against experimental osmotic coefficients and liquid densities, the objective function (OF) for error minimization is given by:

$$OF = \sum_{i=1}^{NP} \left(\frac{\phi_i^{calc} - \phi_i^{\exp}}{\phi_i^{calc}} \right)^2 + \left(\frac{\rho_i^{calc} - \rho_i^{\exp}}{\rho_i^{calc}} \right)^2 \quad (4)$$

where, ϕ_i^{calc}, ρ_i^{calc} are calculated osmotic coefficients and densities, respectively and $\phi_i^{\exp}$, and $\rho_i^{\exp}$ are experimental osmotic coefficient and densities, respectively. The symbol NP is the number of experimental data points. Results of the parameter fitting are discussed in chapter 4.

Table 3: Ion groups used in parameter fitting. Numbers in parenthesis represent the order in which parameter fitting is carried out.

Cations	Anions	
	Cl^- (1)	SO_4^{2-} (4)
Na^+ (1)	(1)	(4)
K^+ (1)		
Mg^{2+} (2)	(2)	
Ca^{2+} (2)	(3)	

3.2. Membrane, pump, turbine and pressure exchanger modules

3.2.1. Membrane module

A model for bench-scale PRO simulation is presented here. This model considers the effects of internal concentration polarization (ICP), external concentration polarization (ECP) and reverse salt permeation to predict the fluxes across a given membrane. After the bench scale model is validated against experimental data, the concepts of bench scale model are extended to full scale PRO process simulation.

For an idealized membrane that is perfectly impermeable to solute and suffers from no fouling or internal or external concentration polarization and can withstand any pressure, the water flux, J_w , is limited by the ability of the membrane to allow water molecules to pass through (permeability coefficient, A), effective osmotic pressure difference ($\Delta\pi_m$) and the applied hydraulic pressure difference (ΔP) [61] across the membrane and is given by equation (1).

Since no membrane is perfectly semi-permeable in reality, a small amount of salt will leak to the feed solution side due to presence of solute concentration differential across the membrane, and is given by equation (5) [20, 62] where B represents the salt permeability coefficient of the membrane active layer and $C_{D,m}$ and $C_{F,m}$ are the active layer interface concentrations of the draw and feed side, respectively.

$$J_s = B\left(C_{D,m} - C_{F,m}\right) \tag{5}$$

This salt leakage and the semi-permeable nature of the membrane causes various performance limiting phenomena in the support layer and at the active layer of the membrane. Initiating the discussion on the performance limiting phenomena in the support layer, it is noted that, as water passes through the membrane from the feed to the draw solution due to osmotic pressure difference, feed salts are selectively retained by the semipermeable active layer and they build up within the porous support layer, resulting in internal concentration polarization. This results in build-up of local concentration at the porous support layer, $C_{F,m}$, when compared to bulk feed solution concentration, $C_{D,m}$, as it can be seen from Figure 7. Diffusion works to

restore this increase in concentration but is hindered by the support layer since it acts an unstirred boundary layer.

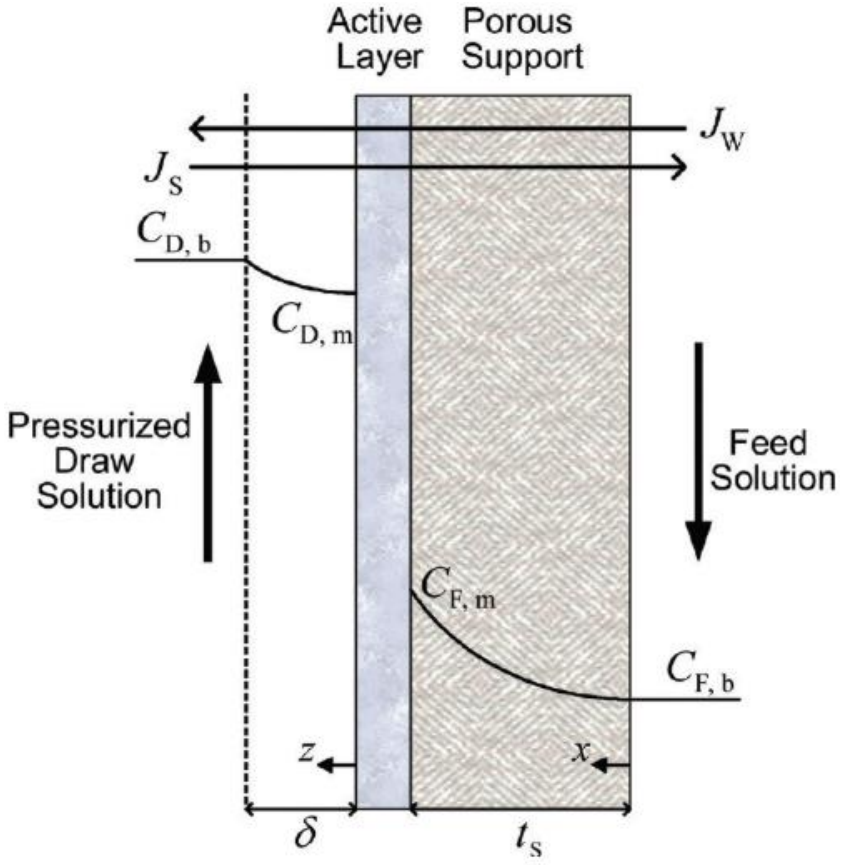

Figure 7: A schematic of concentration profile within a thin-film composite membrane. Reprinted with permission from [35]. Copyright 2011 American Chemical Society

Hence, the resultant salt flux across the porous support arises from diffusion, driven by solute concentration gradient, and convection, arising from the bulk flow of water through the membrane and is given by equation (6) [20], where D^s is the effective diffusion coefficient of the draw solute in the porous support. It is shown that effective diffusion coefficient can be

related to the bulk diffusion coefficient, D as given by equation (7) [62] where, ε and τ are the porosity and tortuosity of the support layer, respectively.

$$J_s = D^s \frac{dC(x)}{dx} - J_w C(x) \tag{6}$$

$$D^s = \frac{D\varepsilon}{\tau} \tag{7}$$

At steady-state, the solute fluxes across the active, Eq (5), and support, Eq (6) layers are equal. Equating both equations and integrating with the boundary condition over the support layer thickness, from x=0, where the salt concentration is the bulk concentration $C_{F,b}$, to x=t_s, where the salt concentration is $C_{F,m}$, results in:

$$C_{F,m} = C_{F,b} \exp\left(\frac{J_w S}{D}\right) + \frac{B}{J_w}\left(C_{D,m} - C_{F,m}\right)\left[\exp\left(\frac{J_w S}{D}\right) - 1\right] \tag{8}$$

where $S = t_s \tau / \varepsilon$ is the support layer structural parameter [63]. Yip et al. [35] assumed in the derivation of equation (8) that external concentration polarization at the feed solution side does not contribute significantly when compared to the internal concentration polarization (ICP) in the support layer due to support layer thickness.

Analyzing equation (8) reveals that the concentration at the active support layer interface, $C_{F,m}$, is the sum of two terms. The first term describes the effect of ICP to the bulk concentration, $C_{F,b}$, where the bulk concentration is amplified by the exponential term. The second term describes the increase in solute concentration at the membrane interface due to the reverse permeation of draw solute into the porous support layer.

Similar performance limiting phenomena occur at the membrane active layer as well, where, as water passes through the active layer from the feed solution to the draw solution, it

dilutes the draw solution at the active layer surface, resulting in external concentration polarization (ECP). Similar to ICP, the solute flux in the ECP boundary layer is given by:

$$J_s = D^s \frac{dC(z)}{dz} - J_w C(z) \tag{9}$$

Following a similar derivation procedure as for equation (8) at equilibrium, but with boundary condition for ECP at the active layer, where the solute concentration is $C_{D,m}$ at z=0 and solute concentration is $C_{D,b}$ at z= δ , the equation for solute concentration at the interface, $C_{D,m}$ is given by:

$$C_{D,m} = C_{D,b} \exp\left(-\frac{J_w}{k}\right) + \frac{B}{J_w}\left(C_{D,m} - C_{F,m}\right)\left[1 - \exp\left(-\frac{J_w}{k}\right)\right] \tag{10}$$

It can be seen that the draw interface concentration $C_{D,m}$ is the sum of two terms, the first term corrects the bulk draw concentration with the ECP factor which rises due to water flux. The second term corrects for reverse solute flux across the active layer.

Since $C_{F,m}$ and $C_{D,m}$ are interface concentrations and are impossible to measure experimentally, Yip et al. [34] subtracted equation (10) from (8) which resulted in:

$$C_{D,m} - C_{F,m} = \frac{C_{D,b} \exp\left(-\frac{J_w}{k}\right) - C_{F,b} \exp\left(\frac{J_w S}{D}\right)}{1 + \frac{B}{J_w}\left[\exp\left(\frac{J_w S}{D}\right) - \exp\left(\frac{J_w}{k}\right)\right]} \tag{11}$$

Applying van't Hoff approximation where the effective osmotic driving force, $\Delta\pi_m$, is proportional to $\Delta C_m = C_{D,m} - C_{F,m}$ The water and reverse salt flux equations are given by:

$$J_w = A\left[\frac{\pi_{D,b}exp\left(-\frac{J_w}{k}\right)-\pi_{F,b}exp\left(\frac{J_wS}{D}\right)}{1+\frac{B}{J_w}\left\{exp\left(\frac{J_wS}{D}\right)-exp\left(\frac{J_w}{k}\right)\right\}}-\Delta P\right] \quad (12)$$

$$J_s = B\left[\frac{C_{D,b}exp\left(-\frac{J_w}{k}\right)-C_{F,b}exp\left(\frac{J_wS}{D}\right)}{1+\frac{B}{J_w}\left\{exp\left(\frac{J_wS}{D}\right)-exp\left(\frac{J_w}{k}\right)\right\}}-\right] \quad (13)$$

where, $\pi_{D,b}$ and $\pi_{F,b}$ are the bulk osmotic pressures of the draw and feed solutions, respectively, and are calculated by the Q-electrolattice EoS employed in the development of this model. The calculation procedure for osmotic pressure determination is outlined in the thermodynamic modelling section.

For the bench scale module, the feed and draw flow rates are significantly larger than the permeate flow rate across the membrane. Hence, the bulk concentration of the draw and feed streams are assumed to be constant along the membrane area.

The water permeate flux J_w given by equation (12) is used to calculate the power density $\dot{W}/A_m$ of the membrane at bench scale given by:

$$\frac{\dot{W}}{A_m} = J_w \times \Delta P \tag{14}$$

The developed bench scale model is verified against experimental data published in the literature and is discussed in the results chapter. A computer program written in FORTRAN is developed and the calculation procedure is initiated by guessing J_w and evaluating equation (12) such that $J_W = f(J_w)$ and the error between the left hand side (L.H.S) and the right hand side (R.H.S) of the equation (12) has reached a pre-specified criterion. The Broyden numerical method [64] was used for faster convergence. The procedure is summarized in Figure 8.

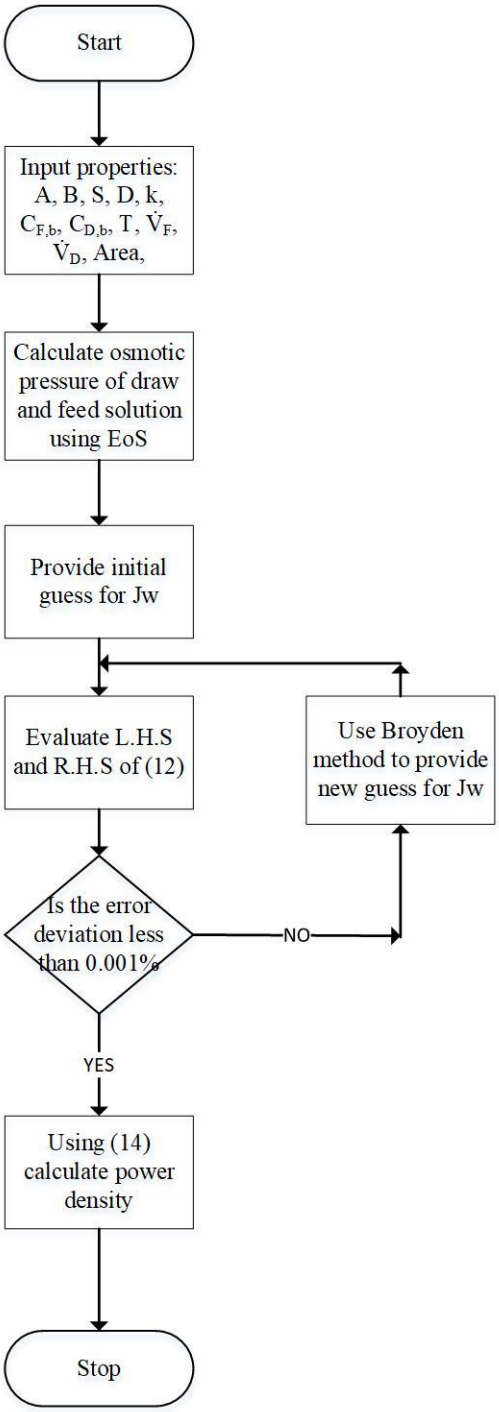

Figure 8: Methodology of solving PRO model for a bench-scale simulation.

For a bench scale simulation, variation along the membrane's is often neglected due to difficulty in observing the variations at small membrane samples. Moreover, since the permeate flux for a bench scale membrane is very small, there is no significant change in concentration of the draw and feed streams during the process hence making it feasible to ignore the variations. But for a full scale membrane, variations along the membrane becomes a significant contributor to the overall performance of the membrane and the PRO process. Variations along the membrane can be either accounted for by taking an average of inlet and outlet variables, or by modeling the membrane using a finite difference approach. A combination of the two approaches is used in this work and is elaborated below. A few assumptions were made during the derivation of the full-scale membrane:

- No pressure drop along the membrane
- Isothermal condition, draw inlet temperature is the same as draw outlet temperature and feed inlet temperature is the same as feed outlet temperature.
- Variation in geometry of the membrane, for a given area, does not result in change in the overall flux calculated. This assumption is based on assuming perfect distribution of flow (for a given flowrate) within the membrane module regardless of its geometrical dimensions, for a given area.

Given these variations along the membrane, water permeate flow rate, $\dot{V}_p$, is calculated by integrating J_w along the membrane.

$$\dot{V}_p = \int_0^a J_w dA_m \tag{15}$$

where A_m is the area of the membrane and $a = A_m$ is the boundary condition based on the variations along the membrane. Volumetric flowrate of water is converted to molar flowrate using the molar volume of the solution given by the EoS.

Similarly the reverse salt molar flux for a full scale membrane is given by:

$$\dot{n}_{p,s} = \int_0^a J_s dA_m \tag{16}$$

And for a full-scale simulation the membrane power density is given by equation (17) where $\dot{W}_{pump}$ and $\dot{W}_{turbine}$ are shaft power of pump and turbine respectively.

$$\frac{\dot{W}}{A_m} = \dot{W}_{pump} + \dot{W}_{turbine} \tag{17}$$

Once the water flux and reverse salt flux are determined across the entire membrane, mass balance on the components on the draw and feed side are carried out. The draw side mass balance is given by:

$$\dot{n}^D_{w,in} + \dot{n}^{J_w}_w = \dot{n}^D_{w,out} \tag{18}$$

$$\dot{n}^D_{i,in} - \dot{n}^{J_s}_i = \dot{n}^D_{i,out} \tag{19}$$

where $\dot{n}^{J_w}_w$ is the molar flowrate of water permeating from the feed side to draw side and $\dot{n}^{J_s}_i$ is the molar flowrate of solute ion i permeating from the draw side to the feed side. Similarly, the mass balance for the feed side of the membrane is given by:

$$\dot{n}^F_{w,in} - \dot{n}^{J_w}_w = \dot{n}^F_{w,out} \tag{20}$$

$$\dot{n}^F_{i,in} + \dot{n}^{J_s}_i = \dot{n}^F_{i,out} \tag{21}$$

A finite difference approach is used to solve eqs. (15) - (21). The membrane module is divided into discrete elements along the membrane and the mass transfer equations for each of these elements are solved simultaneously using boundary conditions, such that the individual solutions of the elements ensure continuity with the inter-element boundaries and the total solution of the differential equation. This technique of discretization also establishes the connectivity of the elements, since each element is solved within the domain of the solution assuming perfect mixing on each side of the membrane. This leads to establishment of counter or co current configuration of the flow within the membrane as shown by Figure 9a and 9b, respectively.

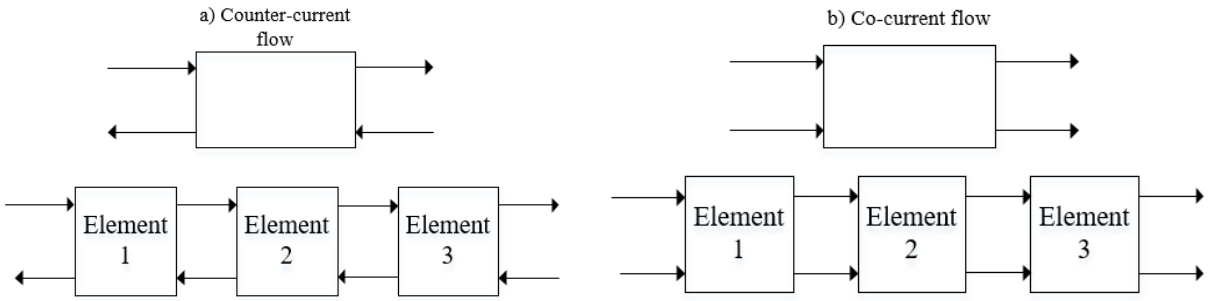

Figure 9: a) Counter-current b) Co-current.

For co-current flow configuration, the system of equations ((15) - (21)) is solved for a discrete element j. Using the solution for water and salt permeate, flowrates and concentrations at the membrane element j+1 are then calculated and the process is repeated until the solution for all the elements, n, is obtained. A schematic of intermediate element calculation is shown in Figure 10 and a summary of the outlined procedure is presented in Figure 11.

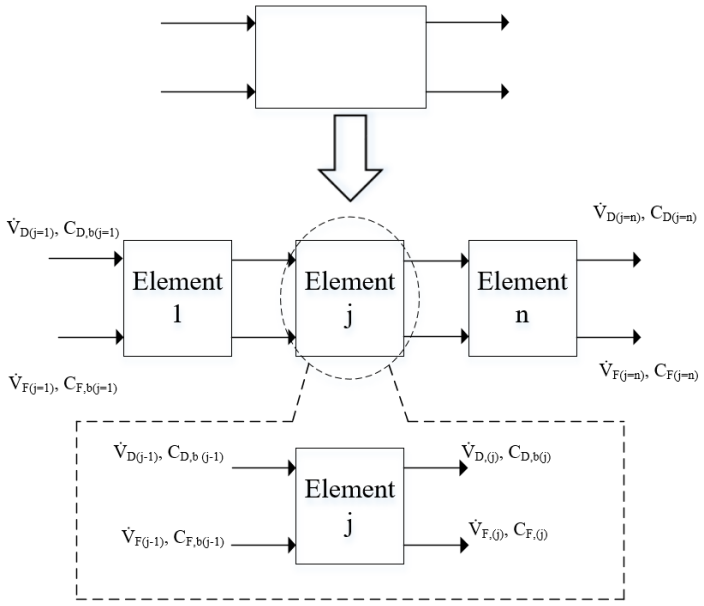

Figure 10: Co-current element intermediate calculation.

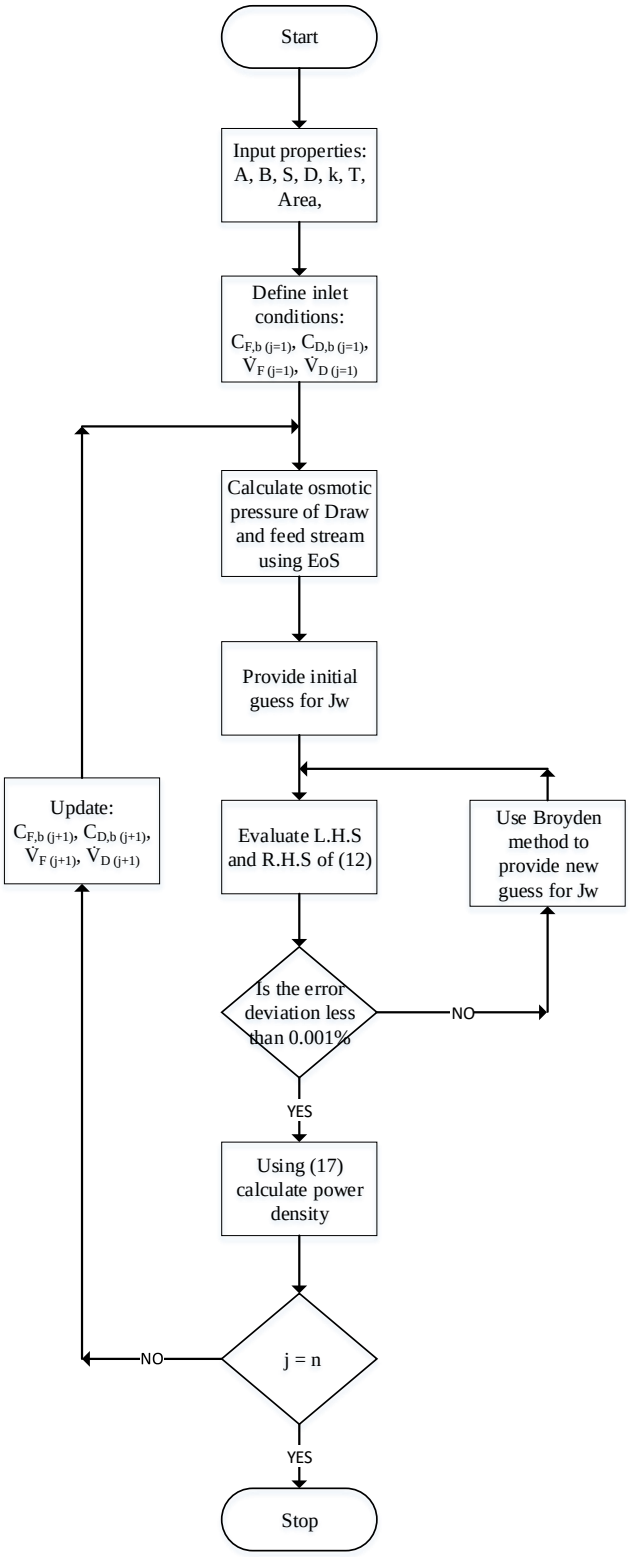

Figure 11: Flow chart for solving co-current flow configuration taking into account variations along the membrane.

For counter-current flow configuration an extra step is required since dividing the membrane module into discrete elements leads to realization of the unknown stream properties in between the elements. This issue is addressed by having an outer nested loop that carries out error analyses between the guessed streams and calculated streams. Referring to Figure 9a, the calculation procedure for counter-current flow configuration is initiated as follows:

1. For an n-element membrane, n-1 inter-element streams on the feed sides are guessed.
2. Equations (15) - (21) for each element are solved simultaneously using the Broyden numerical method and new calculated values for n-1 streams for a n-element membrane is determined.
3. Error comparison between the guessed n-1 and calculated n-1 feed streams is performed using equation (22).
4. If the error has not satisfied the pre-specified criterion then Wegstein numerical method [65] is used to provide new guesses for n-1 streams and the steps are repeated from step 2 until the error criterion is satisfied.

The equation used in the Wegstein method to solve for the inter-element streams is as follows:

$$\begin{aligned} \dot{n}_{w,c}^{F} - \dot{n}_{w,g}^{F} &= 0 \\ \dot{n}_{i,c}^{F} - \dot{n}_{i,g}^{F} &= 0 \end{aligned} \tag{22}$$

where $\dot{n}_{w,c}^{F}$ is the molar flowrate of water of the calculated n-1th stream and $\dot{n}_{w,g}^{F}$ is the molar flowrate of water of the guessed n-1th stream. The symbols $\dot{n}_{i,c}^{F}$ and $\dot{n}_{i,g}^{F}$ refer to the molar flowrate of the ions in the n-1th stream of the calculated and guessed streams, respectively. The error criterion for convergence is set to 0.1%. for equations (22). A schematic of intermediate

stream calculation is shown in Figure 12 and a summary of the outlined iterative procedure is presented in Figure 13.

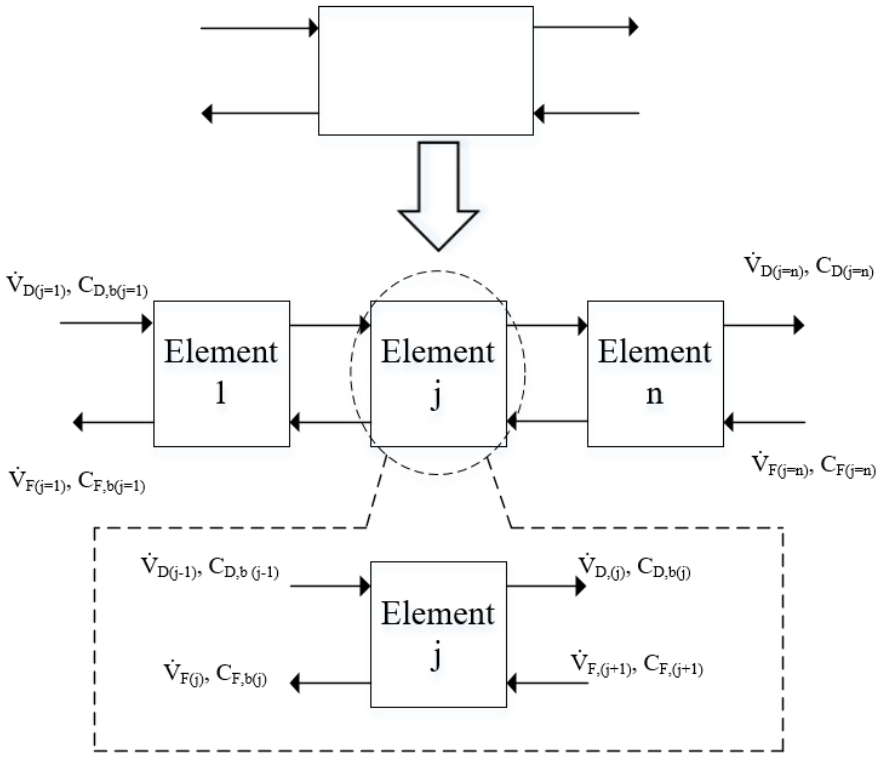

Figure 12: Counter-current inter-element calculation schematic.

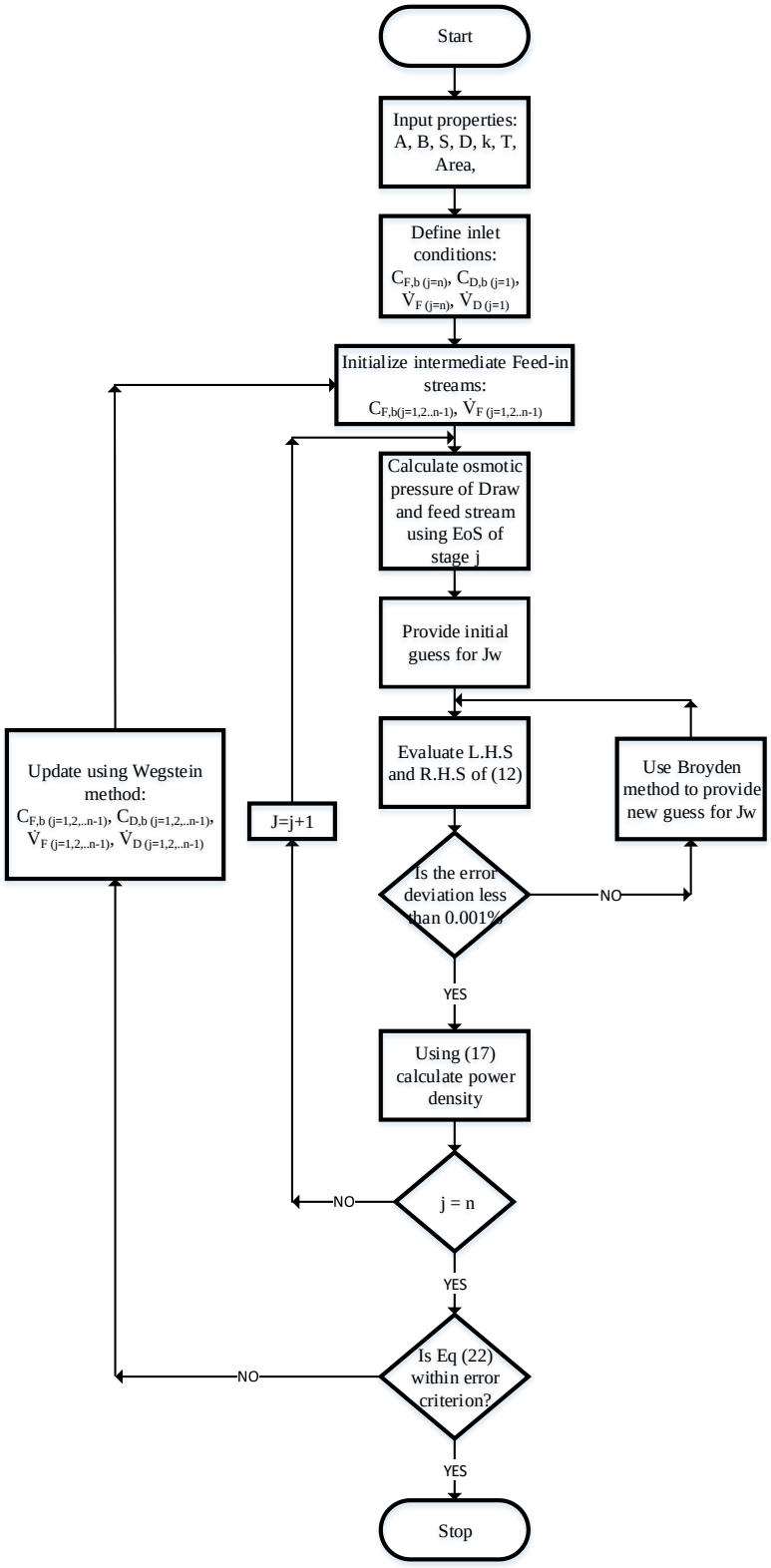

Figure 13: Flow chart for solving counter-current flow configuration taking into account axial variations.

Use of the discrete element approach also leads to determining how many elements are sufficient for an accurate representation of a membrane. This approach is similar to connecting an infinite number of continuous stirred tank reactors (CSTRs) in series to simulate a plug flow reactor. To do that, it was decided to compare the net energy values (turbine energy output minus the pump energy input for adiabatic and reversible conditions) after every element was added. When the inclusion of an additional element led in a net energy deviation of less than 0.1%, compared to the previous case, the number of elements was deemed as appropriate for a full membrane unit simulation. A sample case with the conditions and properties presented in Table 4 and 5 is simulated.

Table 4: Stream conditions.

Conditions	**Draw**	**Feed**
Flowrate (m^3/s)	$4.1x10^{-4}$	$3.84x10^{-4}$
Na^+ concentration (g/L)	94.41	13.79
Cl^- concentration (g/L)	145.59	21.27
Pressure (bar)	60	2.15
Temperature (K)	298.15	298.15

Table 5: Membrane properties.

Area	30 m^2
Water permeability coefficient (A)	0.4 $L/m^2.h.bar$
Salt permeability coefficient (B)	0.3 $L/m^2.h$
Structural parameter (S)	$7.02x10^{-4}$ m
Mass transfer coefficient (k)	138.6 $L/m^2.h$

Figure 14 shows the deviation of the net energy output with respect to the discrete elements of the membrane. Dividing the membrane into 3 elements, the error is 0.121% which is slightly above the criterion set earlier. But with additions of elements 4 and 5 the error is 0.0478% and 0.028%, respectively. This shows that either 4 or 5 elements can be chosen to represent a full scale membrane for the given example. Another key factor that went into deciding the number of discrete elements was the time taken for each simulation to converge. Due to highly iterative nature of the membrane module, every addition of an element increased the convergence time significantly. Hence, it was decided to use 4 discrete elements to represent this particular membrane since the error is lower than the criterion and the convergence time is sufficient for the purpose of our simulation.

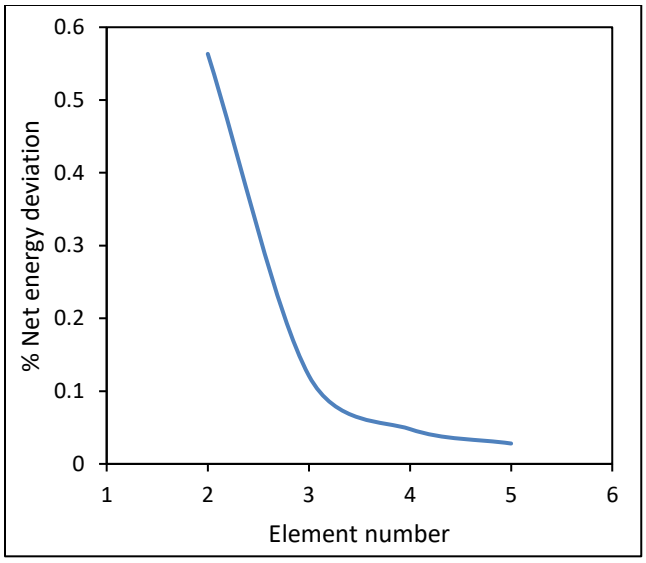

Figure 14: Net energy deviation vs number of elements.

3.2.2. Pump module

To model a pump, it is initially assumed that the pump operates adiabatically and reversibly at steady state condition with no changes in potential and kinetic energy. The modeling is based on the first law of thermodynamics for open systems, given by equation (23), where h, e_k, e_p are the molar enthalpy, kinetic energy and potential energy of the system, respectively, $\dot{Q}$ is the heat transfer rate to the system, $\dot{W}_{shaft}$ is the shaft power required by the pump and $-P\frac{dV_{system}}{dt}$ is the change in volume of the system with time. Based on the assumptions mentioned, Equation (23) simplifies to Equation (24).

$$\frac{d\left[\dot{n}\left(U+E_k+E_p\right)\right]_{system}}{dt}=\sum_{in}\left[\dot{n}\left(h+e_k+e_p\right)\right]_{in}-\sum_{out}\left[\dot{n}\left(h+e_k+e_p\right)\right]_{out}-P\frac{dV_{system}}{dt}+\dot{Q}+\dot{W}_{shaft} \quad (23)$$

$$\dot{W}_{shaft} = \dot{n}\left(h_{out} - h_{in}\right) \tag{24}$$

Carrying out an entropy balance on the pump results in Equation (25), where the term $\frac{d\left(\dot{n}s_{system}\right)}{dt}$ is zero due to steady state assumption, $\sum_{sys}\left(\frac{\dot{Q}}{T}\right)$ is also zero due to adiabatic nature of the process and the term $\dot{S}_{gen}$ is also zero because of reversible assumption. This results in Equation (26).

$$\frac{d\left(\dot{n}s_{system}\right)}{dt} = \sum_{in}\dot{n}s_{in} - \sum_{out}\dot{n}s_{out} + \sum_{sys}\left(\frac{\dot{Q}}{T}\right) + \dot{S}_{gen} \tag{25}$$

$$\dot{n}s_{in} = \dot{n}s'_{out} \tag{26}$$

It can be deduced from Equation (26) that an adiabatic and reversible pump operates isentropically. Hence, to satisfy the adiabatic and reversible assumption, Equation (27), where s'_{out} represents the reversible molar entropy out, is solved by specifying the outlet pressure of the pump and iterating on the outlet temperature of the pump.

$$\Delta s = 0 = s'_{out}\left(T'_{out}, P_{out}\right) - s_{in}\left(T_{in}, P_{in}\right) \tag{27}$$

This results in change in enthalpy (work input), based on the adiabatic and reversible assumption and is calculated using Equation (28), where $\left|\dot{W}'_{shaft}\right|$ represents the adiabatic and reversible power required and h'_{out} represents the adiabatic and reversible molar enthalpy out.

$$\left|W'_{shaft}\right| = \dot{n}\left[h'_{out}\left(T'_{out}, P_{out}\right) - h_{in}\left(T_{in}, P_{in}\right)\right] \tag{28}$$

Once the outlet temperature based on adiabatic and reversible assumption is found, it is necessary to relax the assumption of reversible process since no process is truly reversible in nature. The pump efficiency, η_{pump}, is given by Equation (29).

$$\eta_{pump} = \frac{\left|\dot{W}'_{shaft}\right|}{\left|\dot{W}_{shaft}\right|} \tag{29}$$

Once the real power is calculated, knowing the pump efficiency, Equation (28) is re-written as Equation (30), which is then used to find the temperature of the outlet stream that satisfies the energy balance at the specified pressure.

$$\left|\dot{W}_{shaft}\right| = \dot{n}\left[h_{out}\left(T_{out}, P_{out}\right) - h_{in}\left(T_{in}, P_{in}\right)\right] \tag{30}$$

3.2.3. Turbine module

The calculation procedure for a turbine follows same path as the one for pump, the only difference being that instead of work input into the system, work is output from an adiabatic and reversible turbine. The efficiency of a turbine is defined by Equation (31) where, $\left|\dot{W}'_{shaft}\right|$ is the reversible adiabatic power output, which is calculated using Equation (27), and $\left|\dot{W}_{shaft}\right|$ is the real power output by the process determined from Equation (31). The real temperature of the outlet stream is recalculated by satisfying the energy balance given by Equation (30) at a given turbine efficiency.

$$\eta_{turbine} = \frac{\left|\dot{W}_{shaft}\right|}{\left|\dot{W}'_{shaft}\right|} \tag{31}$$

3.2.4. Pressure exchanger

Modeling a pressure exchanger (PX) is similar to modeling a turbine and a pump because fluid depressurization and pressurization occur in different sections of the same unit. The device operates purely on mechanical energy, which is supplied by the high pressure flow and transferred to the low pressure flow. The mechanism of energy transfer is analogous to that of a positive displacement pump, where low pressure fluid is trapped in a cartridge and is then

discharged at high pressure by the force of a high pressure piston. In the case of the pressure exchanger, however, it is the high pressure flow which effectively acts as the piston. This results in brief contact between the high pressure and low pressure flows. Ensuring equal volumetric flowrates of both flows minimizes mixing which arises from this brief contact [66]. The depressurization section is modeled in a similar manner to a turbine, where the outlet pressure of the section is specified and temperature is calculated based on the entropy and energy balances, as mentioned in the previous section. The mechanical power output from the depressurization side is transferred to the pressurization side. Hence, the specification on the pressurization side is similar to that of a pump. The single major difference is that the output pressure is unknown, rather the total work is known based on energy balance.

Implementation of efficiency for the PX is done in a way such that efficiency of each section of the pressure exchanger is considered separately. In the depressurization section, the efficiency is applied in a similar manner to that of a turbine and the real work is calculated. To apply the efficiency to the pressurization section, an entropy balance is carried out and is given by Equation (32).

$$\dot{S}_{in} - \dot{S}_{out} + \dot{S}_{gen} = 0 \tag{32}$$

where $\dot{S}_{gen}$ is the entropy generation rate. It is assumed that a fraction η of the mechanical power $|\dot{W}_{dep}|$ is transferred from the depressurization side accounts for the mechanical power required for pumping, while a fraction $(1-\eta)$ is dissipated as heat that is absorbed by the pumped fluid. Based on this assumption, $\dot{S}_{gen}$ is given by:

$$\dot{S}_{gen} = \frac{\dot{Q}}{T} \tag{33}$$

where:

$$\dot{Q} = (1-\eta) \times \left| \dot{W}_{dep} \right| \tag{34}$$

and T is assumed to be the average temperature between the inlet and outlet streams in the pumping side of PX.

In summary, referring to the stream numbers of Figure 15, the energy and entropy balances applicable to the pumping side of the PX are:

$$\dot{H}_4 = \dot{H}_3 + \left| \dot{W}_{dep} \right| \tag{35}$$

$$\dot{S}_4 = \dot{S}_3 + \frac{(1-\eta) \times \left| \dot{W}_{dep} \right|}{(T_3 + T_4)/2} \tag{36}$$

This results in a set of two Equations ,(35) and (36), which consider efficiency of the pressurization side. These equations allow the calculation of the real properties and conditions of the exiting stream from the pressurization section by iterating on the temperature and pressure of the exit stream simultaneously.

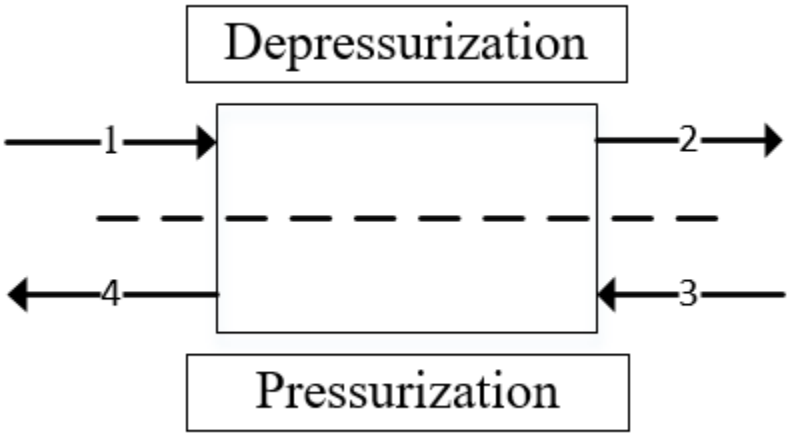

Figure 15: Schematic of a pressure exchanger (PX).

3.3. Thermodynamic modeling

The Q-electrolattice EoS that was used in the development of the process simulator calculates the residual Helmholtz energy function based on the temperature, volume and amounts of water and ions in the solution. Once the Helmholtz energy function is generated, various derivatives are used to calculate the chemical potentials and residual properties such as reduced enthalpy and entropy. From the chemical potentials, it is possible to evaluate the component fugacities and fugacity coefficients.

To calculate the real enthalpies and entropies of the solution, ideal gas properties of the solution are calculated in an external routine and then added to the residual properties as shown by equation (37) and (38).

$$h = h^{ig} + h^{R} \tag{37}$$

$$s = s^{ig} + s^{R} \tag{38}$$

where h^{ig} and s^{ig} are the ideal gas enthalpy and entropy whereas h^{R} and s^{R} are the residual enthalpy and entropy of the solution mixture generated by the EoS, at the same temperature and pressure. To calculate the ideal gas enthalpies and entropies, equations (39) and (40) are utilized.

$$h^{ig}_{i,(T,P)} = h^{ig}_{i,ref\,(T_{ref},P_{ref})} + \int_{T_{ref}}^{T} C_{P,i}\,dT \tag{39}$$

$$s^{ig}_{i,(T,P)} = s^{ig}_{i,ref\,(T_{ref},P_{ref})} + \int_{T_{ref}}^{T} \frac{C^{ig}_{P,i}}{T}\,dT - R\ln\left(\frac{P}{P_{ref}}\right) \tag{40}$$

where, $C^{ig}_{P,i}$ is the molar heat capacity of component ‘i’ at constant pressure. Subscript ‘ref’ refers to the reference state of the system which for the purpose of our calculation is chosen to be a temperature of 303.15 K and a pressure of 101325 Pa. Due to the dependence of molar heat

capacity term on temperature, Equation (41) is used to determine the ideal gas heat capacity at the given temperature, where a, b, c, d, e, are molar heat capacity constants taken from the literature [67].

$$\int_{T_{ref}}^{T} C_{P,i}^{ig} dT = \int_{T_{ref}}^{T} \left(a + bT + cT^2 + dT^3 + eT^4\right) dT \tag{41}$$

Once the ideal gas properties of the components are calculated, a weighted average formula is used to calculate the ideal gas properties of the mixture, as given by equation (42) and (43), where x_i is the mole fraction of the component in the solution.

$$h^{ig} = \sum_{i=1}^{NC} x_i h_i^{ig} \tag{42}$$

$$s^{ig} = \sum_{i=1}^{NC} x_i s_i^{ig} - R \sum_{i=1}^{NC} x_i \ln x_i \tag{43}$$

3.3.1. Osmotic pressure calculation

Based on the discussion provided in the earlier chapters, it can be seen that osmotic pressure calculation is a thermodynamic equilibrium calculation. An electrolyte solution separated by a semi-permeable membrane from a pure solvent, maintained at the same temperature will reach equilibrium when the pressure difference is such that there is no flow of solvent from pure solvent side to the solution side. Hence based on this definition, the fugacity of the solvent in the solution and the pure solvent at the equilibrium is given by:

$$f_s^{\ I} = f_s^{\ II} \tag{44}$$

where $f_s^{\ I}$ and $f_s^{\ II}$ are the fugacity of the solvent in the solution and pure solvent at the same temperature, respectively. Equation (44), when written in terms of its variables, results in:

$$x_s^I \varphi^I_{s,(T_s,P_s^I,x_s^I)} P_s^I = x_s^{II} \varphi^{II}_{s,(T_s,P_s^{II},x_s^{II})} P_s^{II} \tag{45}$$

where φ_s^I and φ_s^{II} are the fugacity coefficients of the solvent in the solution and pure solvent, respectively, x_s^I and x_s^{II} are the mole fraction of the solvent in the solution and in the pure solvent. For the purpose of our calculation the pressure of pure solvent is chosen to be 1atm and equation (45) is then solved for P_s^I such that the equilibrium condition is satisfied. Hence, the osmotic pressure of the solution, Π, in reference to the pure solvent conditions, after the equilibrium condition is satisfied, is given by:

$$\Pi = P_s^I - P_s^{II} \tag{46}$$

Due to iterative nature of the solution to Equation(45), a numerical technique is employed in the program for faster convergence of the osmotic pressure. To initiate the calculation, van't Hoff equation given by Equation (47), where $\varphi_s(T, P_{ref}, x)$ is the fugacity coefficient of the solvent at the given reference pressure of 1 atm, $\varphi_s(T, P_{ref})$ is the fugacity coefficient of the pure solvent at reference pressure of 1 atm , is used to generate initial guess for P_s^I . Then a numerical derivative of the fugacity coefficient, φ_s^I , is taken with respect to P_s^I and equation of a straight line is determined. This is done based on the assumption that the fugacity coefficient behaves linearly at small intervals of pressure. Using the formula derived in the appendix A and presented here, new guesses for the pressures, P_s^I , are generated using Equation (48) until the equilibrium condition is satisfied.

$$P_s^I = -\frac{RT}{V_m^I}\ln\left(\frac{x_s\varphi_s{}^I(T, P_{ref}, x)}{\varphi_s{}^{II}(T, P_{ref})}\right) \tag{47}$$

$$P_{s,i+1}^I = \frac{-x_s^I C_i + \sqrt{\left(x_s^I C_i\right)^2 + 4x_s^I K_i \varphi_s^{II} P_s^{II}}}{2x_s^I K_i} \tag{48}$$

3.3.2. Environment stream property calculation

To fully define a stream in the simulator, properties stated in Table 6 are specified in the input file of the simulator. Once these conditions are specified, the simulator determines the concentration of water molecules that would be needed to make up one liter of solution based on the specified conditions. This is done by guessing the amount of water that would make up a liter of solution, evaluating the compositions of the components ensuring electroneutrality is maintained in the solution, calling the EoS to determine the molar volume of the solution and comparing the calculated volume with the target volume. A flowchart of the outlined procedure is presented in Figure 16.

Table 6: Environment stream specification.

Condition	Units
Temperature	K
Pressure	Pa
Na^+ concentration	(g/L)
Mg^{2+} concentration	(g/L)
Ca^{2+} concentration	(g/L)
K^+ concentration	(g/L)
Cl^- concentration	(g/L)
SO_4^{2-} concentration	(g/L)
Volumetric flowrate	m^3/s

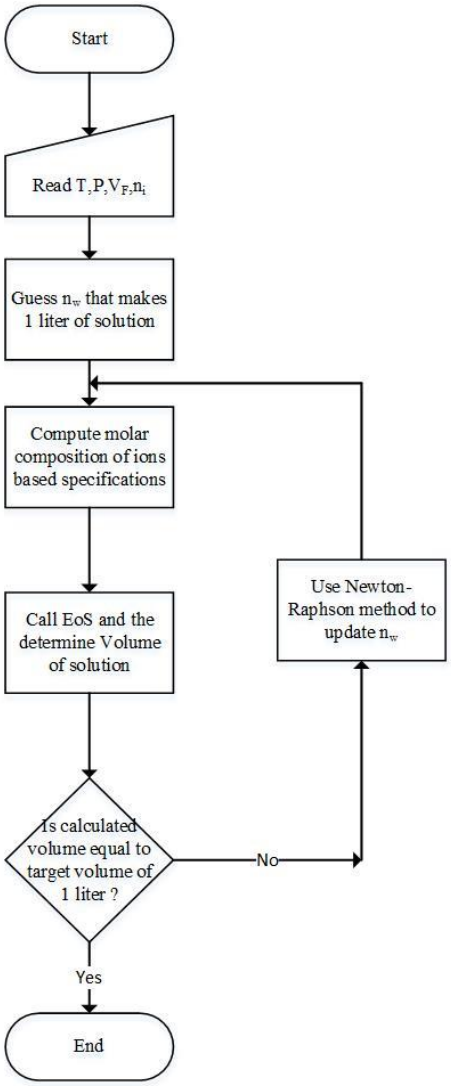

Figure 16: Procedure for inlet stream specification.

To enable fast iterations for calculating the concentration of water in the solution, a Newton-Raphson numerical technique is utilized, where the independent variables is the volume of the solution, V , and the dependent variable is the amount of water in the solution, n_w . The new guesses to solve for the concentration of water is generated by:

$$n_{w,k+1} = n_{w,k} - \left(\frac{dn_w}{dV} \times V_{target} - V_k \right) \tag{49}$$

where, subscript k is the iteration number and $\frac{dn_w}{dV}$ is the numerical derivative taken to provide the next guess to solve for the amount of water. Once the amount of water is obtained, the EoS is finally used to calculate the properties of the stream based on temperature, pressure and composition.

3.4. N-stage implementation

Since one of the goals of this work is to model multi-stage membrane systems, the program is set up such that it can handle such cases. A multi-stage PRO process occurs when there is a change in operating conditions from one membrane to another. This could be either change in operating pressure, change in flow rate of the draw or the feed stream by extracting part of the stream and sending it through a turbine or pressure exchanger or introduction of fresh feed at certain stages. Figure 17 demonstrates an example where the inter-stage operating pressures are manipulated. Such changes in operating conditions introduce a flow-sheet level iteration, adding another layer of iterative calculations that must be satisfied.

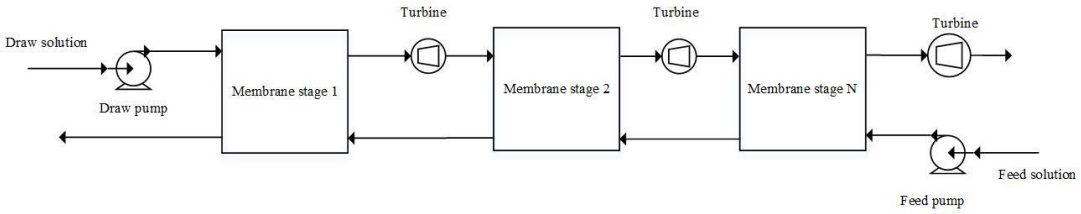

Figure 17: Multi-stage example with variable inter-stage operating pressures

The solving algorithm follows the same steps and numerical methods as mentioned in Figure 13 but with an additional layer of flow-sheet level iteration. The error criterion for solving flow-

sheet level iterations is similar to that of a full scale membrane convergence criterion as given by Equation (22). Summary of flow-sheet level convergence algorithm is given by Figure 18.

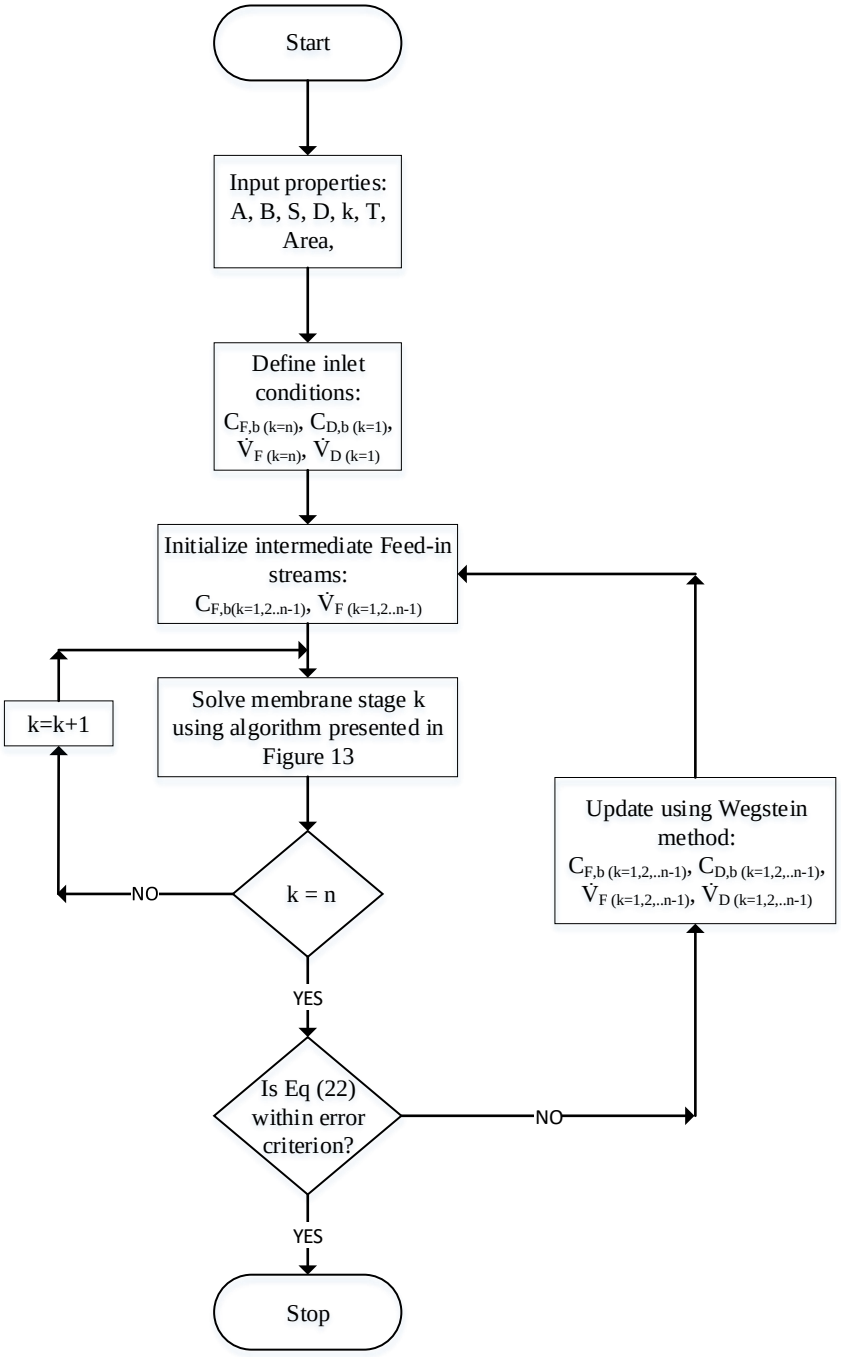

Figure 18: Algorithm for solving N-stage membrane PRO process

3.5. Optimizer implementation

Several parameters affect the performance of a PRO process, such as the applied hydraulic pressure difference (ΔP), area of membrane, flowrate of the draw and feed streams and salinities of the draw and feed streams. Thus, it is convenient to implement an optimizer to find the optimum operating conditions. For the initial step of interfacing the optimizer to the simulator, it is decided to program the optimizer such that it manipulates the area and/or the operating pressures to find the optimum condition. Different criteria are possible, such as achieving maximum power density or the highest net energy recovery.

A simplex method, developed by Nelder and Mead [68] is used for optimizing the parameters. The developed simulator is called as a separate process from within the optimizer. The user loads the PRO process conditions and membrane properties into an input file, the optimizer is run and using the input file from the user, generates the vertices of the simplex and prepares new input files for the simulator. The output from the simulator is stored in a file that has all the stream data including the energy consumed and produced by the process. The optimizer uses the output from the simulator and calculates the net energy output which is the objective function (OF) in this case (given by Equation (50)). The simplex method provides new parameter estimates (operating pressure and/or membrane area depending on the problem specifications) and the iterations continue until convergence is achieved. The methodology is presented in Figure 19.

$$OF = \dot{W}_{shaft,\,pump} + \dot{W}_{shaft,\,turbine} \tag{50}$$

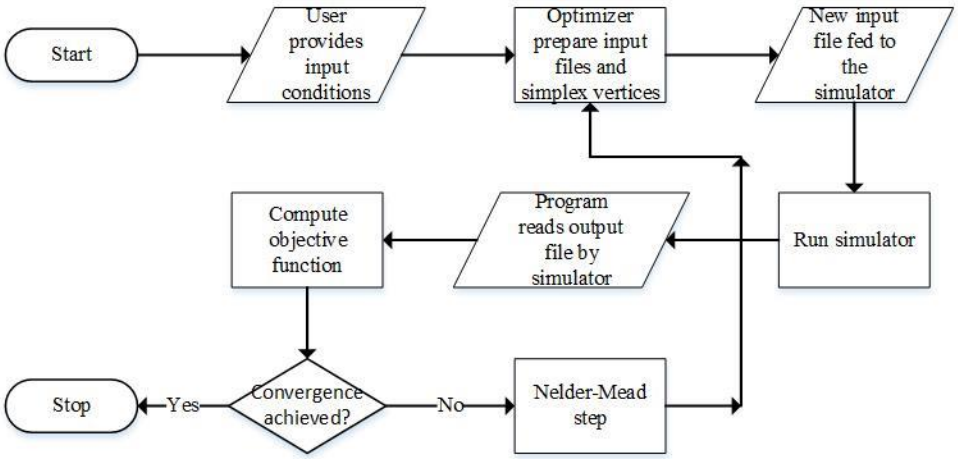

Figure 19: Optimizer methodology. Adapted from [69]

For a single stage PRO process, the operating pressure of the draw stream is manipulated by the optimizer to find the optimum pressure at which the highest net energy is recovered. For a two stage PRO process, the operating pressure of the first stage and second stage are manipulated by the optimizer to find the optimum. And for added complexity, the fractional area split between the 2 membranes is also manipulated such that the total area used for the two stage process remains constant and is the same as the one supplied by the user at the beginning of the optimization. Effectively making the area split fraction between the two membranes as the parameter to optimize. To impose the condition of constant overall area as provided by the user, the optimizer program is modified such that if the area split fraction is greater than 1 or less than 0, the optimizer imposes a very large objective function. Hence ensuring that the split fraction remains between 0 and 1.

3.6. Inputs and outputs of the simulator

Simulation of a PRO process requires numerous user-specified parameters, which are divided into two categories: stream specific parameters and equipment specific parameters. These parameters are consistent with a so-called simulation style problem, where the design specifications of the process input streams and equipment are known and the performance of the process is calculated. Table 7 and 8 presents the inputs and outputs of the simulator, respectively.

Table 7: Inputs of the simulator

Inputs	Units
Draw solution salinity	g/L
Draw solution pressure	Pa
Draw solution flow	m^3/s
Feed solution salinity	g/L
Feed solution pressure	Pa
Feed solution flow	m^3/s
Membrane water permeability (A)	$L/m^2.h.bar$
Membrane Salt permeability (B)	$L/m^2.h$
Membrane mass transfer coefficient (k)	$L/m^2.h$
Membrane structural parameter	m
Membrane area	m^2
Draw solution membrane pressure loss	Pa
Feed solution membrane pressure loss	Pa
Temperature	K
Total pump efficiency	%
Total turbine efficiency	%
Pressure exchanger, depressurization efficiency	%
Pressure exchanger, pressurization efficiency	%

Table 8: Outputs of the simulator

Outputs	Units
Water flux	$L/m^2.h$
Reverse salt flux	$mol/m^2.h$
Net Power	J/s

3.7. Data structure

In any simulator it is necessary to have a data structure that is uniform throughout the entire simulator and is consistent with the inputs and outputs of the equipment. Hence, a master matrix is created that stores all the necessary properties of the streams after the simulation of a given process design is carried out. Table 9 presents the order of the properties that are stored in the master matrix called the PROP matrix. The column in the PROP matrix represents the stream numbers whereas the rows represent the particular property based on the list in Table 9.

Table 9: Order of properties in the PROP matrix

Properties of a given stream	Units
Temperature	K
Pressure	Pa
Flowrate of H_2O	mol/s
Flowrate of Na^+	mol/s
Flowrate of Mg^{2+}	mol/s
Flowrate of Ca^{2+}	mol/s
Flowrate of K^+	mol/s
Flowrate of Cl^-	mol/s
Flowrate of SO_4^{2-}	mol/s
Mole fraction of H_2O	-
Mole fraction of Na^+	-
Mole fraction of Mg^{2+}	-
Mole fraction of Ca^{2+}	-
Mole fraction of K^+	-
Mole fraction of Cl^-	-
Mole fraction of SO_4^{2-}	-
Molar volume of solution	m^3/mol
Molar enthalpy of solution	J/mol
Molar entropy of solution	J/mol.K
Osmotic pressure of solution	bar
Volumetric flowrate	m^3/s
Power	J/s
Molar flowrate	mol/s

4. RESULTS AND DISCUSSION

4.1. Equation of state selection

The chosen EoS (Q-electrolattice and eSAFT-VR-Mie) are compared by re-optimizing the parameters based on the same experimental data set for osmotic coefficients and liquid solution densities. The percent absolute average relative deviation (AARD) between the experimental data and model calculations for liquid densities and osmotic coefficients are calculated and presented in Table 10 and 11.

Table 10: Absolute average relative deviation between experimental data and model calculations for liquid density

Density						
System (Salt + water)	Np*	Mmax† (mol/kg)	T (K)	Ref	AARD (%)	
					Q-electrolattice	eSAFT-VR-Mie
NaCl	140	6.01	273.15-373.15	[70]	0.18	0.53
KCl	120	3.78	273.15-373.15	[70]	0.09	0.69
$MgCl_2$	56	5.00	288.15-328.15	[71]	0.53	0.38
$CaCl_2$	56	6.00	288.15-328.15	[71]	0.44	0.64
Na_2SO_4	120	2.22	273.15-373.15	[70]	0.77	0.68
K_2SO_4	57	0.64	273.15-373.15	[70]	0.17	0.59
$MgSO_4$	106	2.92	273.15-353.15	[70]	1.26	0.46

*Np is the number of experimental data points. †Mmax is the maximum molality examined

Table 11: Absolute average relative deviation between experimental data and model calculations for osmotic coefficient at 298.15 K

Osmotic coefficient					
System (Salt + water)	Np*	Mmax† (mol/kg)	Ref	AARD (%)	
				Q-electrolattice	eSAFT-VR-Mie
NaCl	35	6.00	[71]	1.49	1.12
KCl	20	4.50	[71]	0.62	0.84
$MgCl_2$	17	3.00	[71]	4.38	4.06
$CaCl_2$	16	2.50	[71]	2.95	2.88
Na_2SO_4	19	4.0	[72]	8.59	4.34
K_2SO_4	7	0.7	[72]	5.20	10.53
$MgSO_4$	17	3.0	[73]	21.20	14.27

*Np is the number or experimental data points. †Mmax is the maximum molality examined

Based on the results displayed in Table 10 and 11, there is no overwhelming superiority of an EoS over the other. Given that Rahman [67] has already used the Q-electrolattice EoS and the mass transfer model in his Excel-based simulator, which was validated against literature data, the same modeling options were retained in this work. Nonetheless, the simulator that was developed in this work is modular and it is straightforward to include other EoS and mass transfer models.

4.2. Comparison of simulator results with Excel implementation

After implementing all the modules in the FORTRAN simulator successfully, the results of the simulator were compared with an Excel implementation that utilized the same mass transfer, EoS, pump and turbine models. These Excel results had already been verified against literature data and can be found in [67]. Figure 20 shows the schematic diagram of the simulation conducted on FORTRAN simulator. Table 12 and 13 shows the operating conditions and membrane properties used in the simulation.

Table 14 presents the results of the simulation. The results from the FORTRAN simulator, when compared to the Excel implementation, have deviations that are less than 0.012% for all properties.

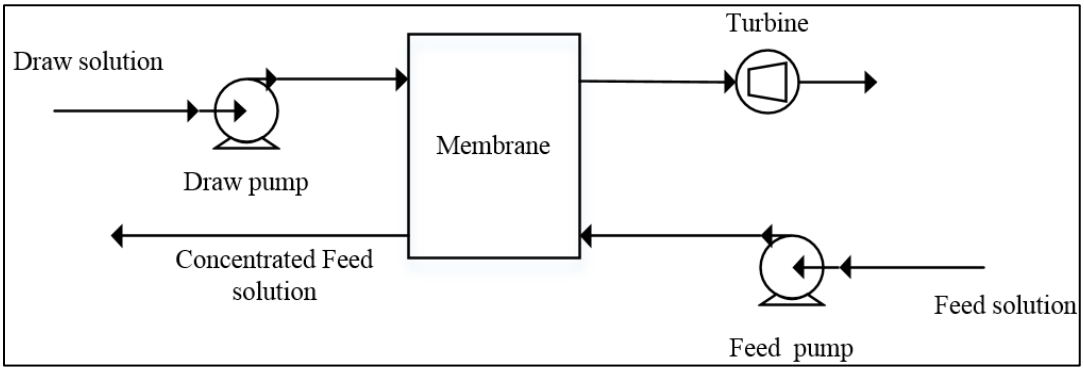

Figure 20: Single stage schematic

Table 12: Operating conditions

Property	Draw	Feed
Flowrate (m^3/s)	0.005	0.005
Inlet temperature (K)	298.15	298.15
Inlet Pressure (bar)	70.0	1.01
Na^+ concentration (g/L)	40.15	10.8
Mg^{2+} concentration (g/L)	2.42	1.29
Ca^{2+} concentration (g/L)	14.07	0.416
K^+ concentration (g/L)	1.62	0.387
CL^- concentration (g/L)	90.22	19.50
SO_4^{2-} concentration (g/L)	6.90	2.71

Table 13: Membrane properties

Area (m^2)	1.00
Water permeability ($L/m^2.h.bar$)	1.77
Salt permeability coefficient ($L/m^2.h$)	0.3
Structural parameter (m)	$7.02x10^{-4}$
Diffusion coefficient (m^2/s)	$1.48x10^{-9}$
Mass transfer coefficient ($L/m^2.h$)	138.6

Table 14: FORTRAN simulator results

Property	FORTRAN simulator	Excel Implementation
Outlet pump temperature (K)	298.30	298.30
Inlet molar volume (m^3/mol)	$1.75x10^{-5}$	$1.75x10^{-5}$
Osmotic pressure (atm)	143.71	143.68
Water flux, J_w ($L/m^2.h$)	6.41	6.41
Sale flux, J_s ($mol/m^2.h$)	0.17	0.17
Pump work (J/mol)	-120.36	-120.34

4.3. Comparison of bench scale PRO results with experimental data

To further validate the results generated by the simulator for the bench scale PRO, various experimental results are compared against the model predictions using membranes of different properties and streams at different temperatures. Table 15 and 16 present the operating conditions and membrane properties that were obtained from previous experimental work conducted by Kim and Elimelech [28] which were conducted at input streams temperature of 20°C. The concentration of draw solution for experiment 1 was 0.5 M NaCl and the feed solution was deionized water (DI) while the draw solution concentration for experiment 2 was 1.0 M NaCl and the feed solution was deionized water. In the simulator the concentration of other ions are set to $1x10^{-20}$ g/L when simulating for NaCl solution, and concentration of all ions are set to $1x10^{-20}$ g/L for simulation of DI water. This is done because the inputs to the simulator are concentration of all ions shown in Table 2 and setting them to a very low number when these ions are not present in the solution effectively renders their effect negligible on the solution properties.

Table 15: Operating conditions of experiments conducted by Kim and Elimelech [28]. Adapted from [28]

Property	Experiment 1		Experiment 2	
	Draw	Feed	Draw	Feed
Flowrate (m^3/s)	$8.33x10^{-6}$	$8.33x10^{-6}$	$8.33x10^{-6}$	$8.33x10^{-6}$
Inlet temperature (K)	293.15	293.15	293.15	293.15
Na^+ concentration (g/L)	11.49	~0.0	22.99	~0.0
Cl^- concentration (g/L)	17.73	~0.0	35.45	~0.0

Table 16: Membrane properties of experiments conducted from Kim and Elimelech [28]. Adapted from [28]

	Experiment 1	**Experiment 2**
Area (m^2)	$2.002x10^{-3}$	$2.002x10^{-3}$
Water permeability ($L/m^2.h.bar$)	1.23	1.23
Salt permeability coefficient ($L/m^2.h$)	2.62	2.62
Structural parameter (m)	$6.89x10^{-4}$	$7.3x10^{-4}$
Diffusion coefficient (m^2/s)	$1.47x10^{-9}$	$1.48x10^{-9}$
Mass transfer coefficient ($L/m^2.h$)	310.32	310.32

Figure 21 and 22 show both the experimental data and model predictions for water flux (J_w) and power density (W/m^2) for conditions used in experiments 1 and 2 with respect to hydraulic pressure difference. In addition to the predictions of the model developed in this work, Figure 21 and 22 includes the results of the simulation carried out by Kim and Elimelech [28], who used OLI Systems, Inc. (Morris Plains, NJ), for osmotic pressure calculation and the mass transfer model developed by Yip et al. [35] for water flux and power density calculations. It can be seen that the results of our simulator are in very good agreement with the experimental data for both water flux and power density. The deviations seen at hydraulic pressure of 12.5 bar for experiment 1 and 12.6 bar for experiment 2 are because of damage to the membrane when operated at high hydraulic pressure difference. The consequence of this damage is that it inherently changes the membrane properties and such change is not part of the mathematical model.

Validation of the optimizer predictions is carried out for the conditions of experiment 1 using the simulator. This validation ensures that the optimizer program has been successfully interfaced with simulator to carry out optimization routines. The result from Figure 21 shows that the optimizer program determined the correct hydraulic pressure at which the optimum power density is achieved for the given process conditions and membrane properties. This successful implementation enables us to carry out optimization in an automated fashion in which the optimum, based on the power density curve is calculated by the optimizer, instead of running the simulator manually at different operating pressures and generating power density curves.

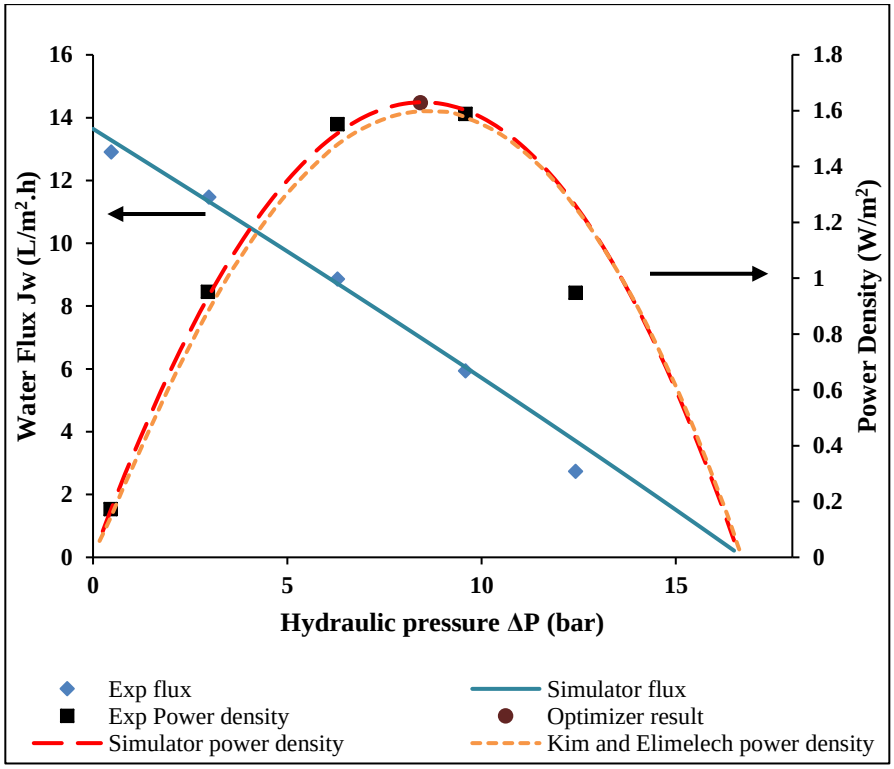

Figure 21: Water flux (J_w) and power density (W/m^2) predictions using the simulator against results reported in the literature by [28] for conditions of experiment 1. Adapted from [28].

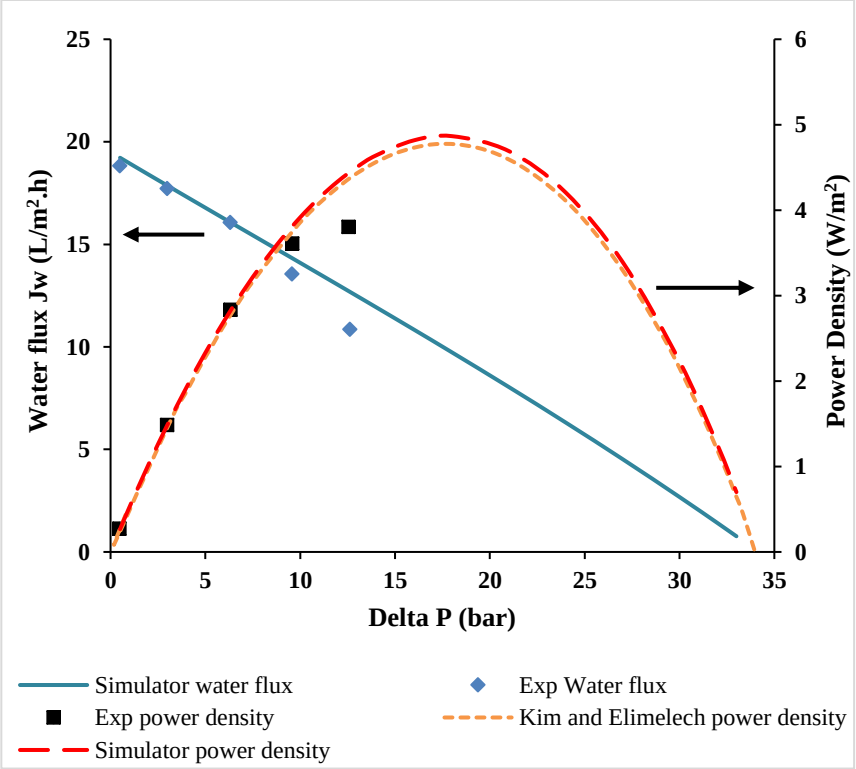

Figure 22: Water flux (J_w) and power density (W/m^2) predictions using the simulator against results reported in the literature by [28] for conditions of experiment 2. Adapted from [28]

To test the reliability of the simulator for predicting water flux and power density at different temperatures, higher concentrations and higher hydraulic pressures, the simulation was run for experimental data reported by Straub et al. [74] for 1 M NaCl, 2 M NaCl and 3 M NaCl draw solutions with deionized water as feed solution at 25°C. Table 17 and 18 shows the operating conditions and membrane properties reported by Straub et al. [74]. Similar to the previous set of simulation runs, the concentration of other salts not present in the solution are set to $1x10^{-20}$ g/L when simulating NaCl draw solution and all salts including NaCl are set to $1x10^{-20}$ g/L when simulating deionized water.

Table 17: Operating conditions of experiments conducted by Straub et al. [74]. Adapted from [74]

Property	Experiment 1		Experiment 2		Experiment 3	
	Draw	**Feed**	**Draw**	**Feed**	**Draw**	**Feed**
Flowrate (m^3/s)	$1.33x10^{-5}$	$2.0x10^{-7}$	$1.33x10^{-5}$	$2.0x10^{-7}$	$1.33x10^{-5}$	$2.0x10^{-7}$
Inlet temperature (K)	298.15	298.15	298.15	298.15	298.15	298.15
Na^+ (g/L)	22.99	~0.0	44.99	~0.0	68.97	~0.0
Cl^- (g/L)	35.45	~0.0	70.91	~0.0	106.36	~0.0

Table 18: Membrane properties for experiments conducted by Straub et al. [74]. Adapted from [74]

Area (m^2)	$2.002x10^{-3}$
Water permeability ($L/m^2.h.bar$)	2.49
Salt permeability coefficient ($L/m^2.h$)	0.39
Structural parameter (m)	$5.64x10^{-4}$
Diffusion coefficient (m^2/s)	$1.48x10^{-9}$
Mass transfer coefficient ($L/m^2.h$)	99.0

Figure 23, 24 and 25 show the water flux and power density of the three experimental runs with respect to hydraulic pressure. These figures also include the simulation results of Straub et al. [74] who used OLI systems, Inc. (Morris Plains,NJ) for osmotic pressure calculation and mass transfer model developed by Yip et al. [35] for water flux and power density calculations. It is worth noting that our simulator uses the Q-electrolattice EoS to predict thermodynamic properties including osmotic pressures. The simulator developed in this work

predicted results that are in very good agreement with the experimental data. Similar to previous example, the optimizer was run for experiments 1 and 3 conditions, listed in Table 17. From Figure 23 and 25, it can be seen that the optimizer predicted the exact hydraulic pressures at which the optimum power density is achieved.

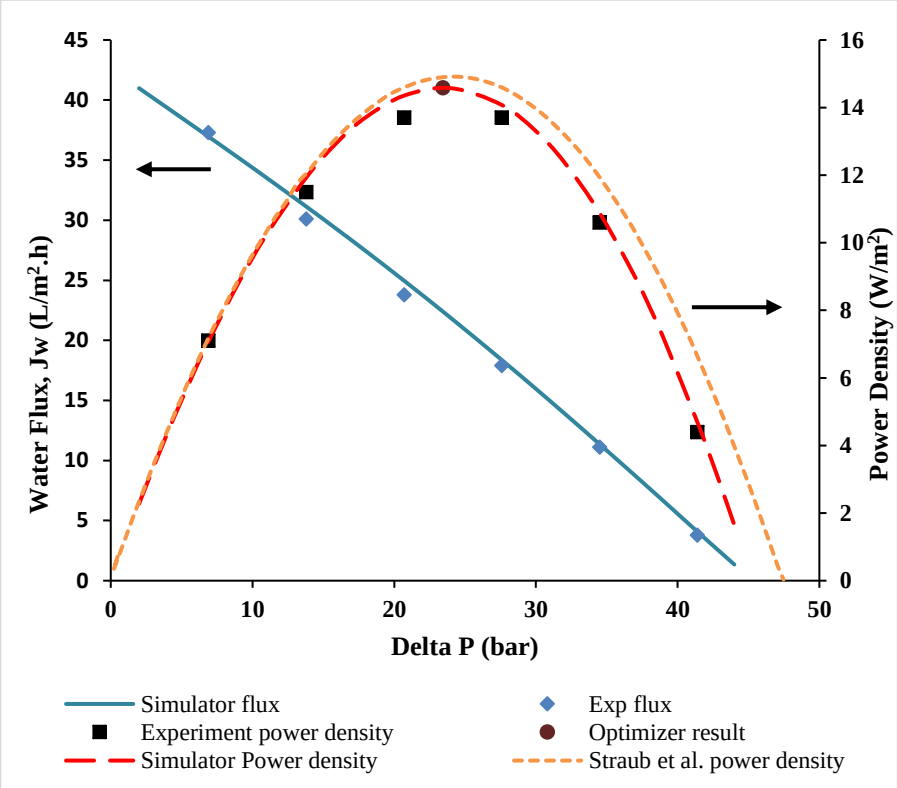

Figure 23: Water flux (J_w) and power density (W/m^2) predictions using the simulator against results reported in the literature by [74], using experiment 1 conditions listed in Table 17. Adapted from [74]

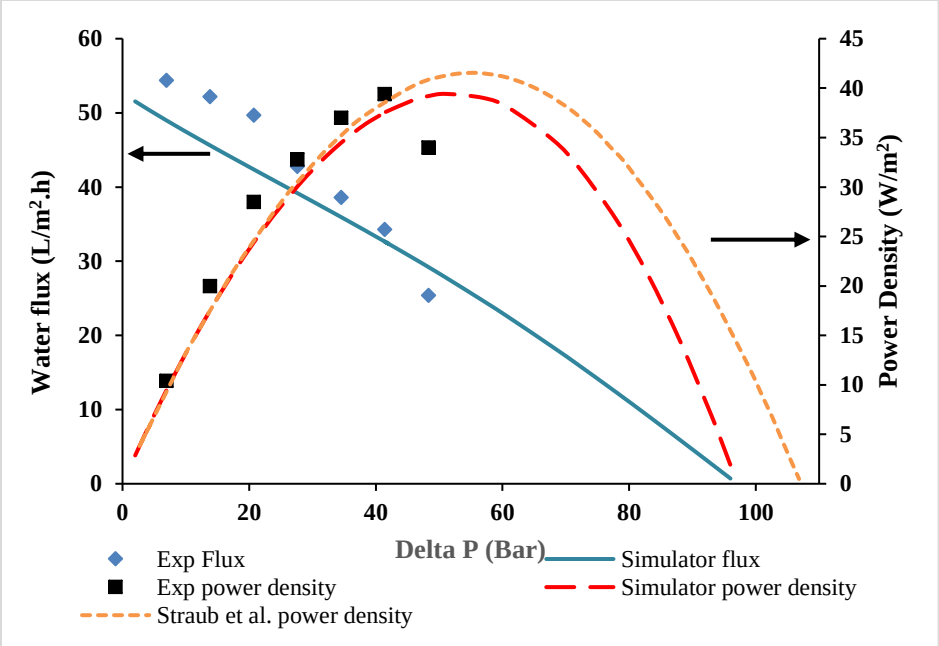

Figure 24: Water flux (J_w) and power density (W/m^2) predictions using the simulator against results reported in the literature by [74], using experiment 2 conditions listed in Table 17. Adapted from [74]

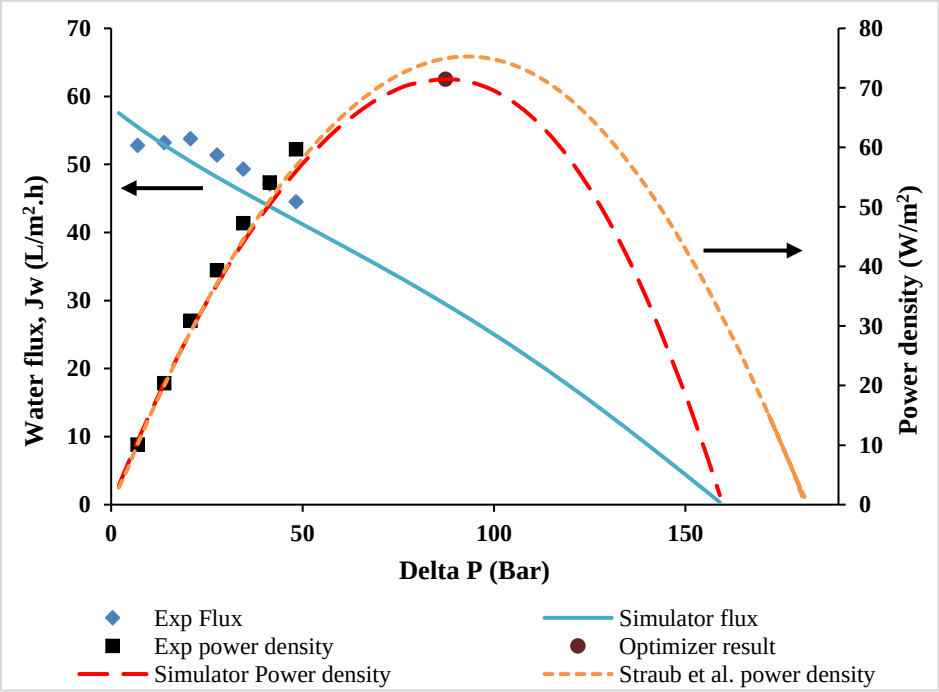

Figure 25: Water flux (J_w) and power density (W/m^2) predictions using the simulator against results reported in the literature by [74], using experiment 3 conditions listed in Table 17. Adapted from [74]

From the results presented in Figure 21 - 25, it can be observed that the simulator developed herein can predict water flux and power density very accurately when compared to the experimental data at bench scale. Also, the results of our simulator agreed very well with results that were reported by Straub et al. The key difference arises when the bench scale model is extended to full-scale simulation, where existing models use a simplified van't Hoff equation for the prediction of osmotic pressure, which is a key driving force in the PRO process.

4.4. Full-scale simulation results

After validating the results of the bench scale simulator with the published experimental data, we extended the capability of the developed mathematical model in order for it to be able to simulate a full-scale PRO process. One key feature that differentiates our approach from the approach other authors have taken to model full-scale membrane units [36-39, 75] is that, in our full-scale implementation, we utilize an EoS for predictions of osmotic pressures rather than using a simplified van't Hoff equation. The implementation of van't Hoff equation that previous researchers have employed is primarily due to its simplicity and makes it easy to be integrated with the finite differences approach that is used for simulating full-scale membrane units. Moreover, the assumption that at low salinities Van 't Hoff equation can predict osmotic pressures with reasonable accuracy is also made by previous researchers [36, 37, 39]. Use of an EoS will provide accurate stream data that otherwise would not be accessible when using van't Hoff equation.

To demonstrate the difference in the predicted specific energy from a full –scale PRO using a simplified van't Hoff equation, when compared to using an EoS, the specific energy (extractable energy) of the membrane was calculated by equation (51) using van't Hoff equation and Q-electrolattice EoS, where $\Delta \dot{V}_p$ is the volume of permeated water across the membrane.

The effect of increasing areas while keeping the feed and draw flowrate constant on the extractable energy is investigated.

$$SE = \frac{\Delta P \Delta \dot{V}_P}{\dot{V}_{F,o} + \dot{V}_{D,o}} \tag{51}$$

Figure 26 and 27 present the simulation carried out for a 0.6M NaCl draw solution paired with 0.015M NaCl feed solution and 2.74M NaCl draw solution paired with 0.6M NaCl feed solution. The hydraulic pressure difference used in the simulations presented in Figure 26 and Figure 27 are 14.5 bar and 56.9 bar, respectively.

The deviations in specific energy extracted can be explained by referring to Figure 28. This figure displays the effect of salt molality on the osmotic coefficients of NaCl solutions at 298.15K along with values calculated using the ideal solution model, van't Hoff equation and the Q-electrolattice EoS. At low molarities, van't Hoff equation tends to over predict the osmotic coefficients when compared to experimental data. On the other hand at high molarities, the van't Hoff equation tends to under predict the osmotic coefficients when compared to experimental data.

These trends are reflected in the simulation of the full-scale membrane units given by Figure 26 (low molarity) and 27 (high molarity). Moreover, as the membrane area per feed flow rate is increased (i.e., increase in membrane area), the deviations become substantial. These deviations are essentially due to the dilution effect in a full-scale membrane, which causes the osmotic pressure difference to vary along the membrane and, due to unreliable predictions by van't Hoff equation, the osmotic pressure difference is not accurately captured.

Hence, the predictions of osmotic coefficients made by the EoS are more accurate at a wider range of molalities than van't Hoff's equation. Because of this, the energies predicted by

the simulator are more reliable. Full-scale simulations like these are generally used to evaluate the potential of a process design, and if the underlying models are able to give accurate predictions of the variation of driving force along the membrane over a wide range of molalities, then these simulation tend to be more trustworthy.

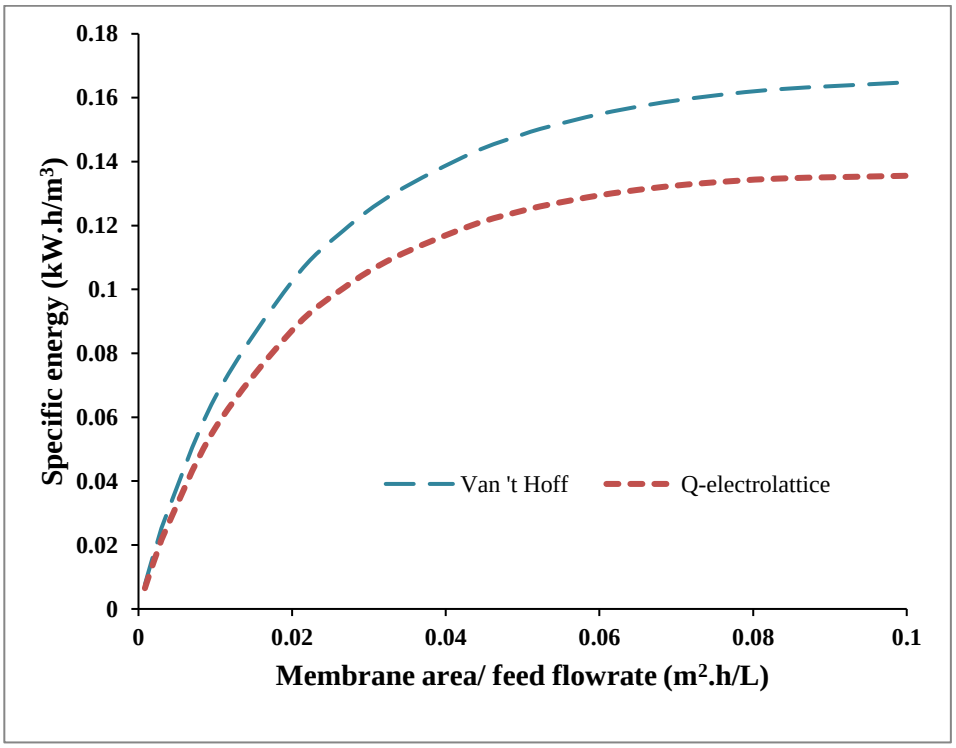

Figure 26: Specific energy vs membrane area/feed flowrate for Seawater (0.6M NaCl) draw solution and river water (0.015M NaCl) as feed solution.

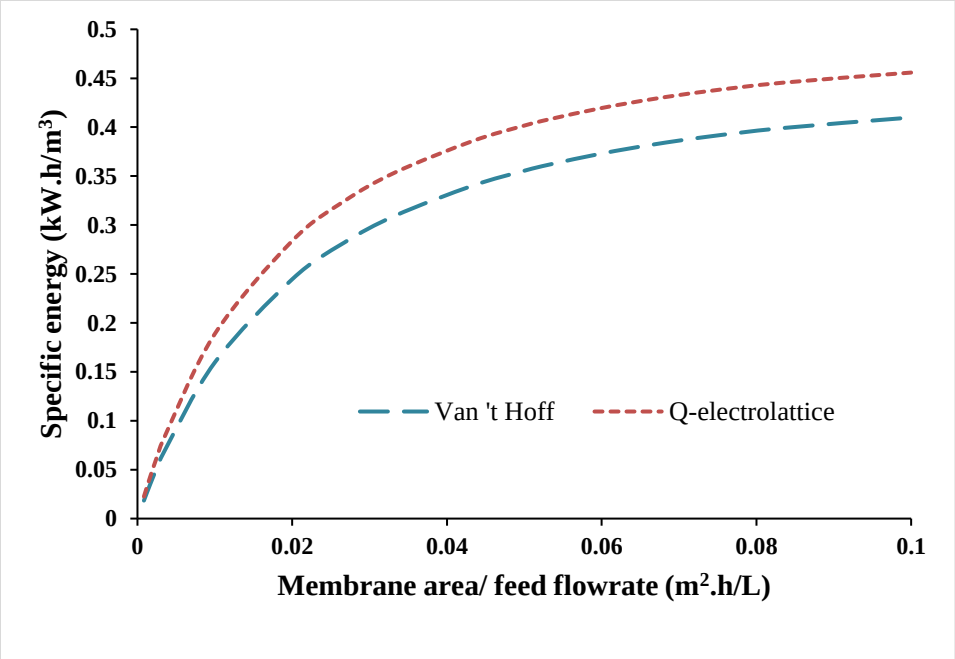

Figure 27: Specific energy vs membrane area/ feed flowrate for high salinity water (2.74M NaCl) as draw solution and seawater (0.6M NaCl) as feed solution.

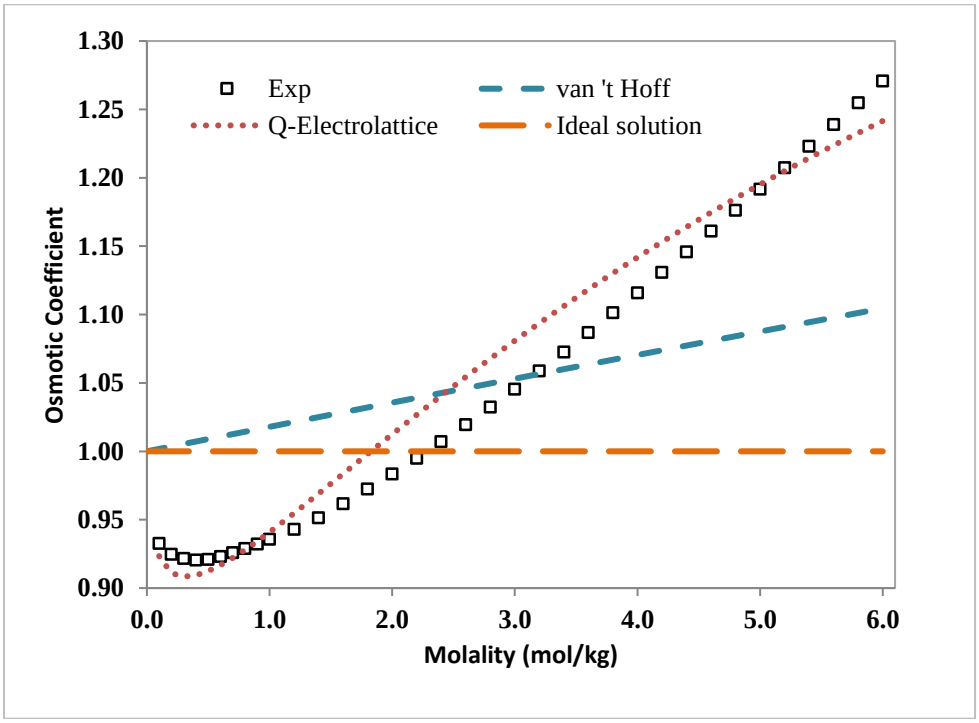

Figure 28: Osmotic coefficients Van 't Hoff, Q-electrolattice and Ideal solution models against experimental data

These observations further justify the use of an EoS suitable for electrolytes for full scale PRO simulations. Next, analyses were carried out on possible flow configurations that could be used in the PRO processes. The co-current and counter current flow configurations were compared to analyze which of the two will result in a higher net energy recovery. The membrane parameters and the process conditions used to simulate the flow configurations are given by the single stage entries presented in Table 19 and 20.

Figure 29 and 30 show the osmotic pressure profiles for draw and feed solutions along the membrane for counter current and co-current flow, respectively. It can be seen from the figures that for a counter current flow configuration, the osmotic pressure difference between the draw and feed streams seems to decrease at a smaller rate compared to the co-current flow configuration, where the osmotic pressure difference is highest at the beginning and then it rapidly decreases along the membrane. To quantify this more rigorously, we define the driving force (DF) in the membrane as follows:

$$DF = \Delta\pi - \Delta P \tag{52}$$

where, $\Delta\pi$ is the osmotic pressure difference and ΔP is the hydraulic pressure difference across the membrane. Since the membrane module is assumed to be a constant pressure module, the effect of variation of osmotic pressure difference along the membrane on the driving force can be observed using this approach. Figure 31 shows the plot of counter-current and co-current driving force profiles along the membrane area. It can be seen that for a co-current flow, the driving force is highest at the start (from the draw side, referring to Figure 10) of the membrane but as the flow progresses, the driving force rapidly diminishes whereas for a counter-current flow the driving force is still obtainable until the end of the membrane. This availability of driving force along the whole membrane results in higher recoverable energy from the PRO

process. For the given simulation, the power density achieved for co-current flow configuration was 12.02 W/m^2 whereas for a counter-current flow configuration the power density attained was 16.26 W/m^2, with a 35 % increase above the co-current configuration. While this numerical result is for the specific case, the observation about the distribution of the driving force is general and indicates that operating a PRO process in counter-current flow configuration results in higher efficiency of the process.

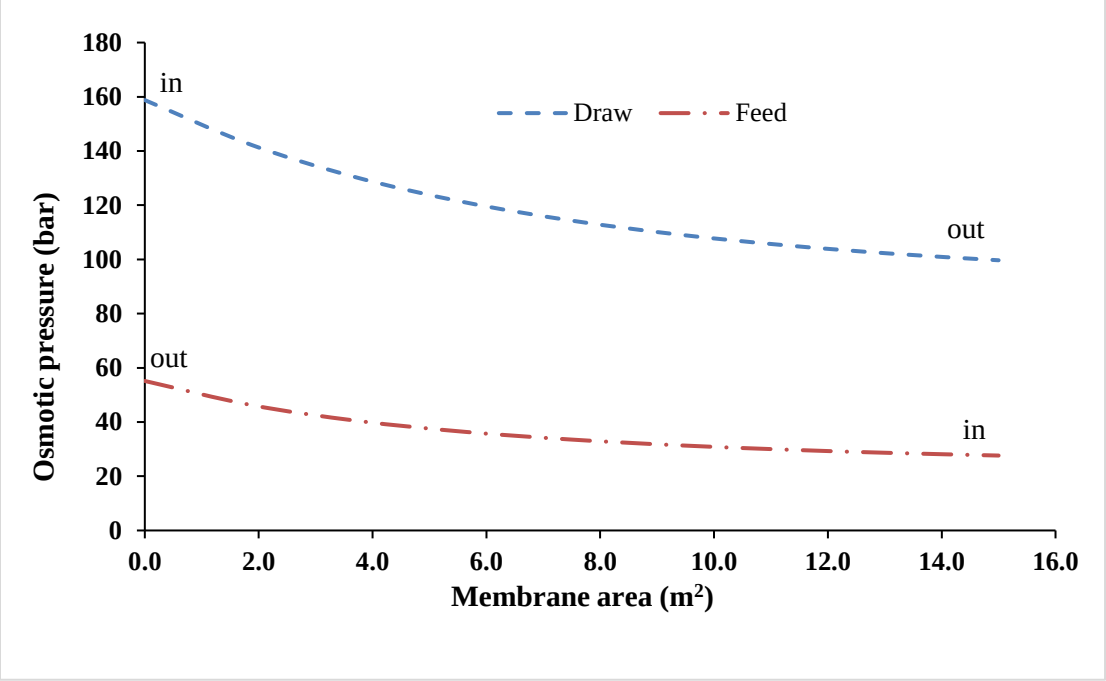

Figure 29: Osmotic pressure profile along the membrane for a Counter-current flow configuration

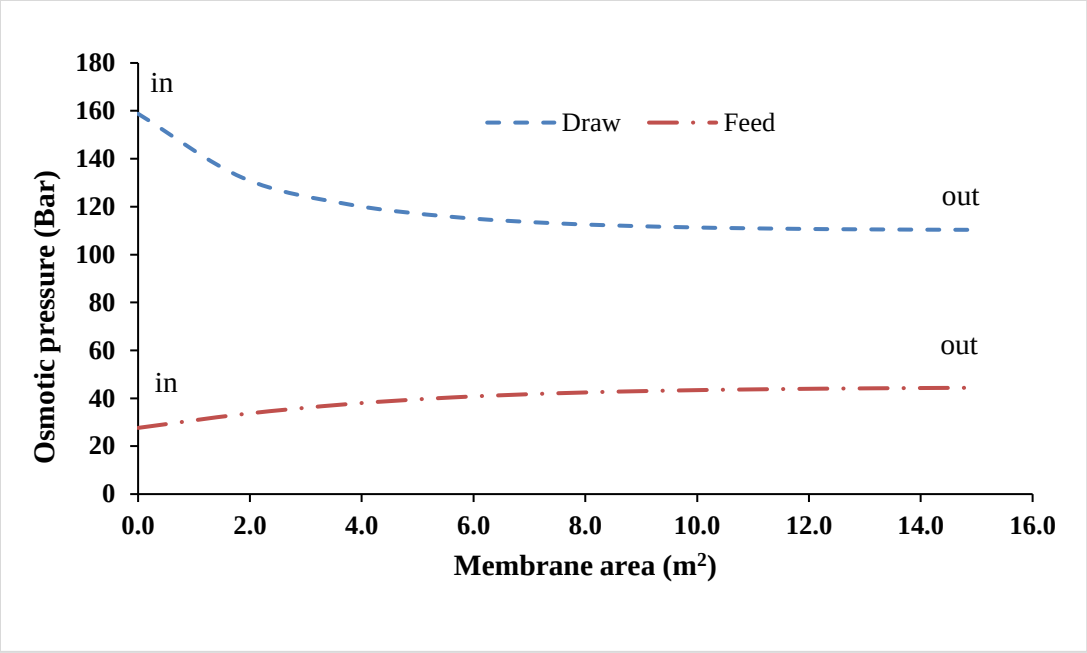

Figure 30: Osmotic pressure profile along the membrane for a co-current flow configuration

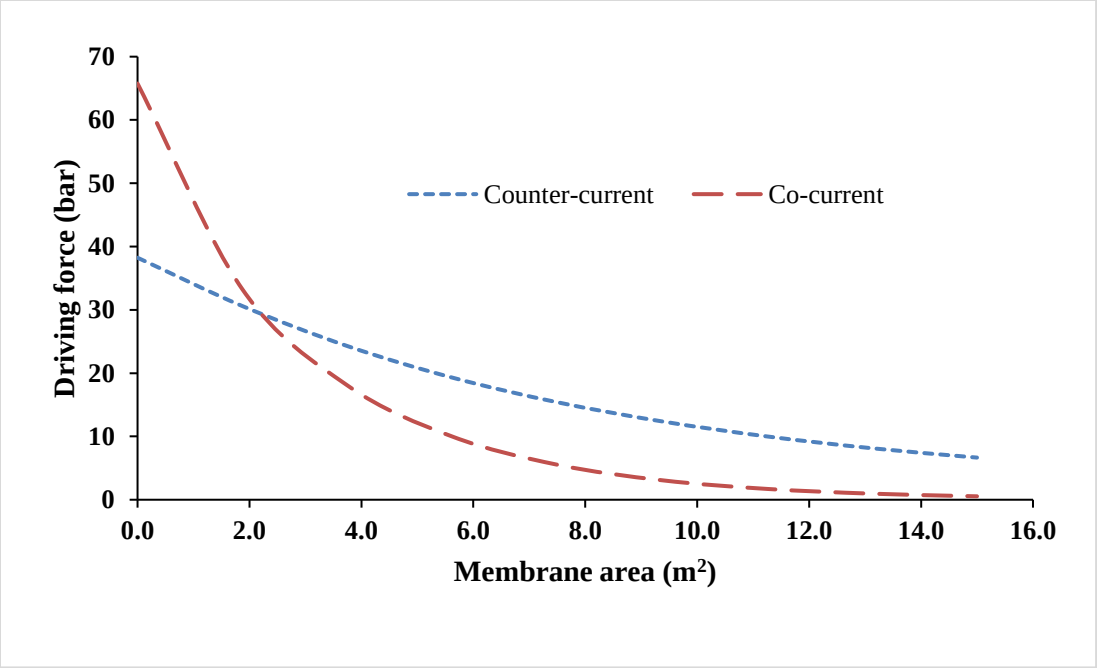

Figure 31: Driving force profile (Δπ -ΔP) along the membrane for a counter-current and co-current flow configuration.

The next step is to extend the analysis to a multistage setup in order to investigate if the use of a staged membrane can further increase the efficiency of the process. For a multi-stage analyses, it is hypothesized that each membrane would have different optimum operating pressure that would result in a higher overall energy recovery for a given draw solution flowrate.

For these analyses, the optimizer tool interfaced with the developed simulator is used to find the optimum for draw pump and inter-stage turbine, as shown in Figure 32 (Scenario 1). For this example, it is assumed that the pumps and turbines operate at 100% efficiency. The initial feed flow rate fraction is manipulated for each optimization run to analyze at which fraction the largest gain in energy recovery can be obtained. For comparison, the optimizer is also run for a single membrane stage PRO process, as shown in Figure 20, utilizing the same process conditions as for the two-stage process. Membrane properties used in the optimization are given in Table 19. The initial draw solution flowrate for all the runs is set at 8.33×10^{-5} m^3/s. Table 20 presents the process conditions for which the initial feed flow rate fraction (Φ) is set at 0.5, where (Φ) = initial feed flow rate/(initial feed flow rate + initial draw flow rate).

Table 19: Membrane properties for a single stage and two-stage simulation

	Single stage	Two stage	
		Stage 1	Stage 2
Area (m^2)	15	7.5	7.5
Water permeability ($L/m^2.h.bar$)	3.0	3.0	3.0
Salt permeability coefficient ($L/m^2.h$)	0.36	0.36	0.36
Structural parameter (m)	$1x10^{-4}$	$1x10^{-4}$	$1x10^{-4}$
Diffusion coefficient (m^2/s)	$1.61x10^{-9}$	$1.61x10^{-9}$	$1.61x10^{-9}$
Mass transfer coefficient ($L/m^2.h$)	138.6	138.6	138.6

Table 20: Process conditions for $\phi = 0.5$ for a single stage and two-stage PRO process.

	Single stage		**Two stage**	
Property	**Draw**	**Feed**	**Draw**	**Feed**
Flowrate (m^3/s)	$8.33x10^{-5}$	$8.33x10^{-5}$	$8.33x10^{-5}$	$8.33x10^{-5}$
Inlet temperature (K)	298.15	298.15	298.15	298.15
Na^+ concentration (g/l)	62.94	13.79	62.94	13.79
Cl^- concentration (g/l)	97.06	21.27	97.06	21.27

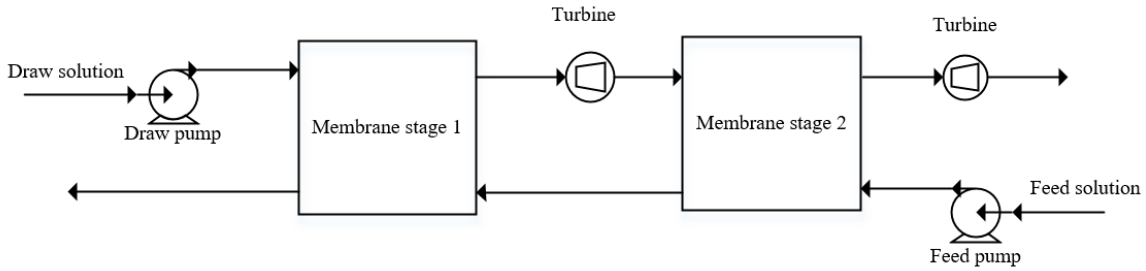

Figure 32: Two-stage membrane PRO process with inter-stage turbine (Scenario 1).

Table 21 shows the results of simulation at different values of Φ. The initial feed flowrate fraction is manipulated and the optimizer is run to find the optimum pressure of the draw pump and inter-stage turbine for two stage membrane PRO process and the optimum pressure of the draw pump for single stage PRO process. The net energy gain is given by:

$$E_{1stage} = \dot{W}_{shaft,pump} + \dot{W}_{shaft,turbine} \tag{53}$$

where $\dot{W}_{shaft,pump}$ is the energy input to the process by the pump and $\dot{W}_{shaft,turbine}$ is the energy output from the process by the turbine.

Table 21: Optimizer results for single stage and two-stage PRO process

ϕ	Total Area (m^2)	Area Split ratio		Optimum Δ P (bar)			Energy extracted (W)			Gain in energy recovery
		Single stage	Two stage	Single stage	Two stage		Single stage	Two stage		$\frac{E_{2stage} - E_{1stage}}{E_{1stage}}$
					Stage 1	Stage 2		Stage 1	Stage 2	
0.4	15	1.0	0.5	68.4	71.3	68.0	216.17	104.55	115.26	0.3%
0.5	15	1.0	0.5	59.4	69.9	56.6	247.05	134.85	124.13	3.56%
0.75	15	1.0	0.5	51.7	70.8	42.5	276.13	186.95	127.59	12.7%
0.85	15	1.0	0.5	49.9	70.2	39.8	281.09	201.61	125.53	15.1%

It can be seen from Table 21 that the optimum pressure for two stage PRO process is different for each stage. In particular, it can be seen that the optimum pressure for the second stage is significantly lower than the optimum pressure of the first stage. This can be explained by the effect of the driving force defined by equation (52). Figure 33, 34 and 35 show the driving force plotted against membrane area for a single-stage membrane and two-stage membrane process for ϕ = 0.5, 0.75 and 0.85. It can be seen from the figures that for a single stage membrane, the driving force keeps decreasing non-linearly along the membrane for a constant pressure operation. But for a two stage process the driving force is rejuvenated for the second stage by the introduction of an inter-stage turbine, and this increase in driving force resulted in higher efficiency of the two-stage membrane process than the single-stage one. This shows that if process conditions for the second stage membrane are manipulated, or more specifically if a change in process conditions is introduced in the second stage such that the process conditions of the first stage are adjusted as well, then the energy extracted from PRO for a given draw solution flowrate can increase.

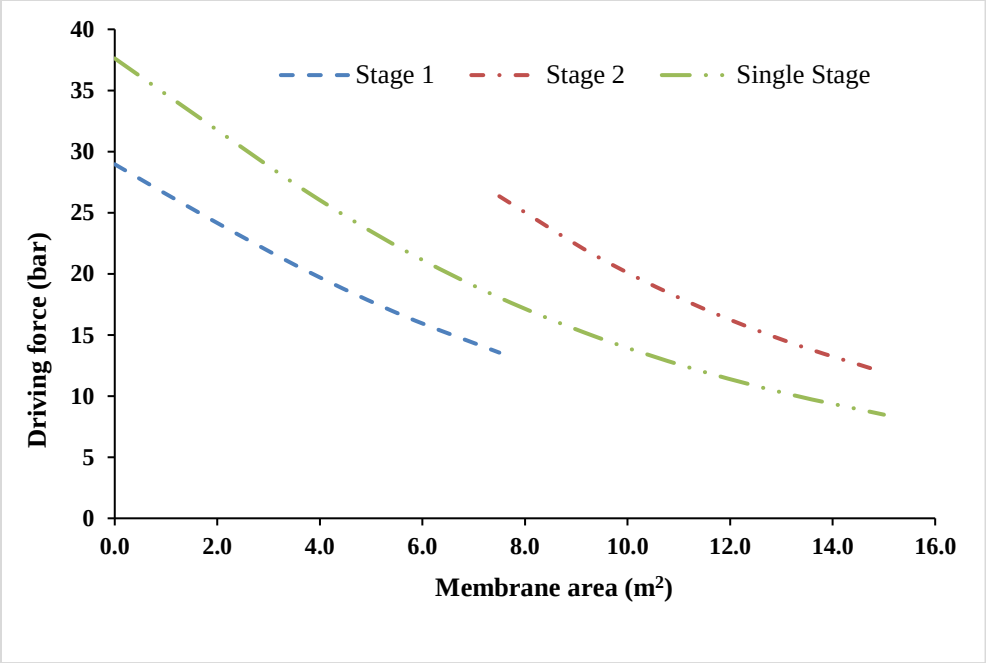

Figure 33: Driving force vs membrane area for Φ = 0.5

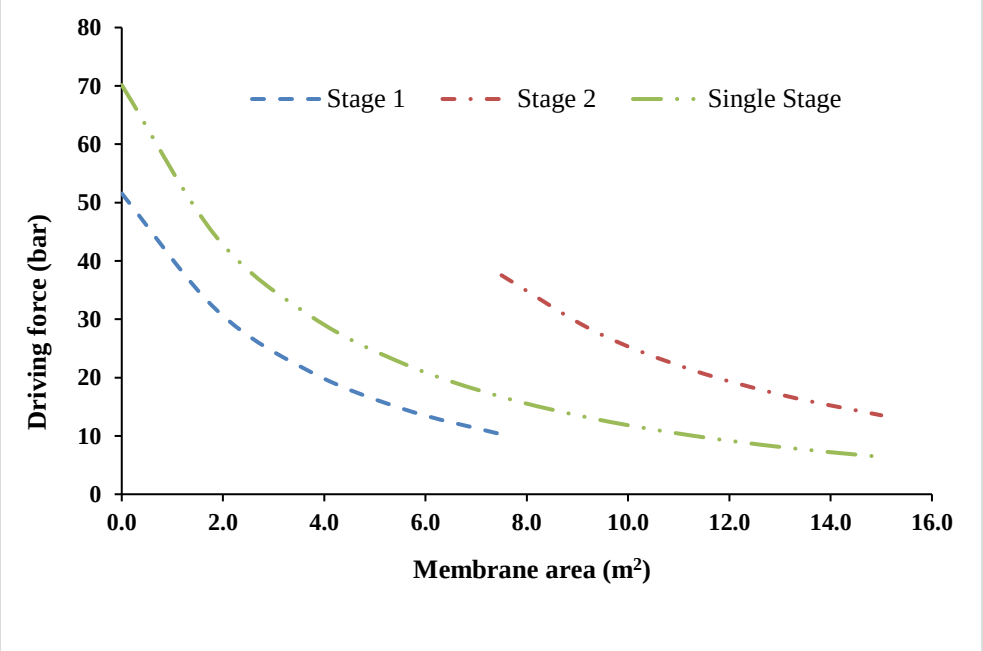

Figure 34: Driving force vs membrane area for Φ = 0.75

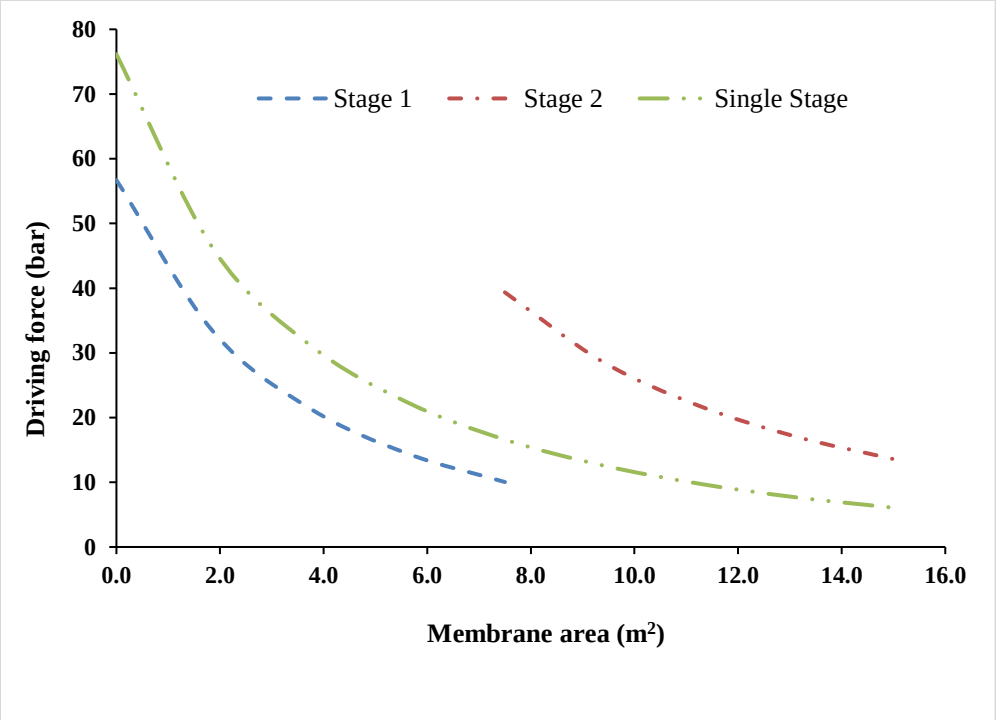

Figure 35: Driving force vs membrane area for Φ = 0.85

The Process configuration in Figure 36 (Scenario 2) is proposed to extract energy from high salinity gradient. The idea behind the proposed configuration is that, split fraction equal to the volumetric flowrate of permeated water would be removed through a side stream and pass through the turbine and the rest of the flow would pass through another turbine to adjust the optimum operating pressure of the second stage. The hypothesis is that the operating pressure of the second stage would be lower than the operating pressure of the process design given in scenario 1 but still be able to recover the same amount of energy or more compared to the initial two-stage design. The membrane properties and process conditions given in Table 19 and 20, respectively, are used in the simulation of both the scenarios. In addition, all the assumptions used in the simulation of scenario 1 (Figure 32) are used in the simulation of scenario 2 (Figure 36).

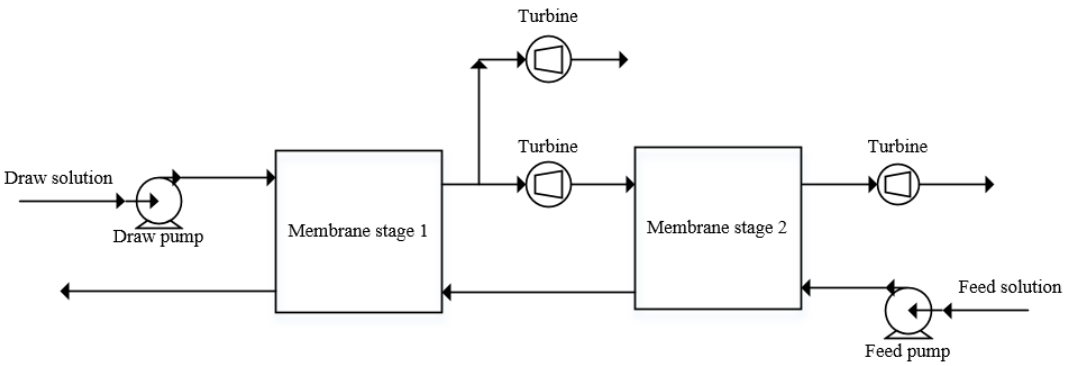

Figure 36: Two-stage PRO process with 2 inter-stage turbine (Scenario 2)

Table 22 shows the results for scenarios 1 and 2 for $\phi=0.5$. It can be seen that the optimum operating pressure for the second stage is lower for scenario 2 than for scenario 1 but the gain in energy recovery when compared to single stage for scenario 2 is lower when compared to scenario 1. This can be explained by the fact that, when part of the flow is taken as a side stream and the rest of the flow is send to the turbine for the second stage, the effect of dilution on this flow is higher compared to when the entire flow from the first membrane is fed to the second membrane. Hence, this effect causes rapid decrease in the driving force in the second stage of scenario 2 compared to scenario 1, therefore leading to a lower recovery of saline energy compared to scenario 1. The effect described can be clearly seen in Figure 37, where the driving force for second stage in scenario 2 rapidly decreases when compared to scenario 1.

Table 22: Optimizer results for scenario 1 and 2

Scenario	Phi	Total Area (m^2)	Area Split ratio		Optimum Delta P (bar)			Gain in energy recovery
			Single stage	Two stage	Single stage	Two stage		$\frac{E_{2stage} - E_{1stage}}{E_{1stage}}$
						Stage 1	Stage 2	
1	0.5	15	1.0	0.5	59.4	69.9	56.6	3.56%
2	0.5	15	1.0	0.5	59.4	71.0	55.4	1.40%

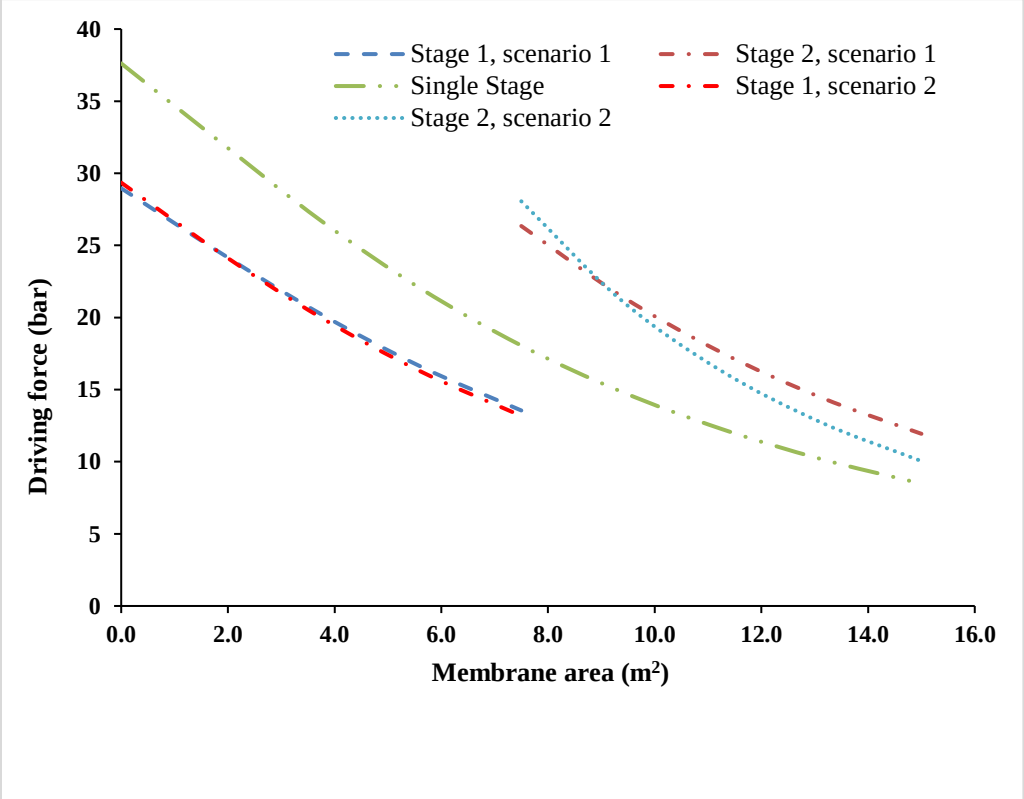

Figure 37: Driving force vs membrane area for scenarios 1 and 2

4.5. Pressure exchanger implementation

The net energy recovered in PRO processes is very sensitive to the efficiency of the pumps and turbines used. The use of pressure exchangers is highly attractive for PRO because of their large efficiencies, compared to pumps and turbines.

Table 23 presents the simulated results for a full-scale PRO process using the process design presented in Figure 20 and 3, respectively. The efficiency of the pumps and turbines were fixed at 74% and 75%, respectively. Efficiency of the pressure exchanger reported in the literature was found to be between 95%-98% [76] and the implementation of efficiency in the developed simulator requires the efficiency specification of the depressurization side and pressurization side, which results in the efficiency based on published data. It can be seen that the implementation of pressure exchanger plays an important role in the amount of energy recovery from PRO as introduction of pump and turbine efficiency resulted in a net power input into the process for a given membrane for the second run. However, as soon as a pressure exchanger is introduced into the process design, for a given membrane, a net power density is recovered from the process. This is attributed to the high efficiency of the pressure exchanger that enables the feasibility of the PRO process.

Table 23: Simulation results taking into account efficiencies of the equipment

Process design	PX η (%)		Pump η (%)	Turbine η (%)	Delta P (Bar)	Area (m^2)	ϕ	Power density (W/m^2)
	De-pressurization	Pressurization						
Figure 20	-		100	100	58.9	15	0.5	16.47
Figure 20	-		74	75	58.9	15	0.5	-7.08
Figure 3	98	97	74	75	58.9	15	0.5	10.58

5. CONCLUSION AND FUTURE WORK

A Pressure Retarded Osmosis (PRO) process simulator incorporating internal concentration polarization (ICP), external concentration polarization (ECP) and reverse solute flux (RSF) for bench scale membranes has been developed and validated with experimental results for 0.6M, 1.0M, 2.0M and 3.0M NaCl draw solutions with deionized water at temperatures of 20°C and 25°C using the Q-electrolattice EoS. The developed mathematical model is extended to plant-scale simulation by using a discretization technique for the membrane (finite difference model). Rigorous equipment models for pump, turbine and pressure exchanger were implemented using the energy and entropy balances. Nelder-Mead based optimizer is successfully interfaced with the simulator for optimization of operating pressures of PRO membranes to achieve the optimum power density for the process.

Plant-scale simulation for high salinity draw solution (2.74M NaCl) with seawater (0.6M NaCl) feed solution has shown that using models available in the literature, which utilize van't Hoff model for osmotic pressure determination for plant-scale simulation, tends to under predict the specific energy extractable between high salinity draw solution and low salinity feed solution pairing. On the other hand, if solution pairing for seawater and river water (0.015M NaCl), the models developed using the van't Hoff equation tend to over predict the extractable energy. This has serious effects when evaluating a PRO process performance, since these erroneous predictions can lead to inaccurate predictions.

Using the optimizer tool on a two stage membrane PRO process has shown that the operating optimum pressure of the second stage is significantly lower than the operating optimum pressure of the first stage. Moreover, the net energy extracted from a two-stage PRO

process is higher compared to a single stage PRO process, operated at their respective optimum pressures.

An example on the importance of pressure exchanger utilization within the PRO process design is demonstrated by running a scenario with equipment efficiencies of pumps and turbines without and with a pressure exchanger implemented in the process design. It was clearly seen that including a pressure exchanger plays an important role in making the PRO process feasible.

The simulator developed herein is based on a mass transfer model that is derived for a flat-sheet membranes. In reality, spiral wound or hollow-fiber membranes are most commonly used in the industry. Hence, a mass transfer model that can take into account ICP, ECP and RSF in the spiral wound membranes should be implemented for further accuracy.

Another suggested future extension of this work is to implement a rigorous costing model that takes into account changes in process conditions, designs and flow configuration. This will help in further evaluating the feasibility of the process, not only in terms of energy recovered, but also in terms of revenue and investment needed.

Moreover, due to mechanical limitations of PRO membranes for handling high pressures, it is worthwhile to explore process designs that would result in a lower operating pressure but still be able to extract high energy from PRO systems. The development of this highly versatile simulator allows such an analysis to be carried out in a streamlined manner.

REFERENCES

[1] W.A. Edelstein, L.C. Davis, M.I. Dearborn, CO2, Kyoto and Energy, in: Panel on Public Affairs, Amercian Physical Society, 2002.

[2] M.I. Hoffert, K. Caldeira, G. Benford, D.R. Criswell, C. Green, H. Herzog, A.K. Jain, H.S. Kheshgi, K.S. Lackner, J.S. Lewis, H.D. Lightfoot, W. Manheimer, J.C. Mankins, M.E. Mauel, L.J. Perkins, M.E. Schlesinger, T. Volk, T.M.L. Wigley, Advanced technology paths to global climate stability: Energy for a greenhouse planet, Science, 298 (2002) 981-987.

[3] S. Chu, A. Majumdar, Opportunities and challenges for a sustainable energy future, Nature, 488 (2012) 294.

[4] S. Hastings-Simon, D. Pinner, M. Stuchtey, Myths and realities of clean technologies, McKinsey & Company. http://www. mckinsey. com/businessfunctions/sustainability-and-resource-productivity/our-insights/myths-and-realities-ofclean-technologies, (2014).

[5] B.E. Logan, M. Elimelech, Membrane-based processes for sustainable power generation using water, Nature, 488 (2012) 313-319.

[6] S. Loeb, F. Van Hessen, J. Levi, M. Ventura, The osmotic power plant, in: 11th Intersociety Energy Conversion Engineering Conference, 1976, pp. 51-57.

[7] N.Y.V. Yip, David A.; Nijmeijer, Kitty.; Elimelech, Menachem., Power Density Analysis of Reverse Electrodialysis Power Generation with Natural Salinity Gradients, J. Environ. Sci. Technol., 48 (2014) 4925-4936.

[8] M.C. Hatzell, R.D. Cusick, B.E. Logan, Capacitive mixing power production from salinity gradient energy enhanced through exoelectrogen-generated ionic currents, Energy Environ. Sci., 7 (2014) 1159-1165.

[9] X. Zhu, W. Yang, M.C. Hatzell, B.E. Logan, Energy recovery from solutions with different salinities based on swelling and shrinking of hydrogels, J. Environ. Sci. Technol., 48 (2014) 7157-7163.

[10] J.W. Post, J. Veerman, H.V. Hamelers, G.J. Euverink, S.J. Metz, K. Nymeijer, C.J. Buisman, Salinity-gradient power: Evaluation of pressure-retarded osmosis and reverse electrodialysis, J. Membr. Sci., 288 (2007) 218-230.

[11] E.M. Kramer, D.R. Myers, Osmosis is not driven by water dilution, Trends Plant Sci., 18 (2013) 195-197.

[12] Blue energy cell mechanism, https://commons.wikimedia.org/wiki/File:Blue_energy_mechanism.png, 2018, (accessed on 18 August 2018).

[13] F. Helfer, C. Lemckert, Y.G. Anissimov, Osmotic power with pressure retarded osmosis: theory, performance and trends–a review, J. Membr. Sci., 453 (2014) 337-358.

[14] A. Tanioka, K. Saito, M. Irie, S. Zaitsu, H. Sakai, H. Hayashi, Power generation by pressure retarded osmosis using concentrated brine from sea water desalination system and treated sewage: review of experience with pilot plant in Japan, The 3rd Osmosis Membrane Summit, 4 (2012) 1-33.

[15] S. Loeb, Large-scale power production by pressure-retarded osmosis, using river water and sea water passing through spiral modules, Desalination, 143 (2002) 115-122.

[16] R. Pattle, Production of electric power by mixing fresh and salt water in the hydroelectric pile, Nature, 174 (1954) 660.

[17] S. Loeb, Production of energy from concentrated brines by pressure-retarded osmosis: I. Preliminary technical and economic correlations, J. Membr. Sci., 1 (1976) 49-63.

[18] G.D. Mehta, S. Loeb, Internal polarization in the porous substructure of a semipermeable membrane under pressure-retarded osmosis, J. Membr. Sci., 4 (1978) 261-265.

[19] G. Mehta, S. Loeb, Performance of permasep B-9 and B-10 membranes in various osmotic regions and at high osmotic pressures, J. Membr. Sci., 4 (1978) 335-349.

[20] K. Lee, R. Baker, H. Lonsdale, Membranes for power generation by pressure-retarded osmosis, J. Membr. Sci., 8 (1981) 141-171.

[21] S. Loeb, T. Honda, M. Reali, Comparative mechanical efficiency of several plant configurations using a pressure-retarded osmosis energy converter, J. Membr. Sci., 51 (1990) 323-335.

[22] S.E. Skilhagen, J.E. Dugstad, R.J. Aaberg, Osmotic power—power production based on the osmotic pressure difference between waters with varying salt gradients, Desalination, 220 (2008) 476-482.

[23] K. Gerstandt, K.-V. Peinemann, S.E. Skilhagen, T. Thorsen, T. Holt, Membrane processes in energy supply for an osmotic power plant, Desalination, 224 (2008) 64-70.

[24] T. Thorsen, T. Holt, The potential for power production from salinity gradients by pressure retarded osmosis, J. Membr. Sci., 335 (2009) 103-110.

[25] A.P. Straub, A. Deshmukh, M. Elimelech, Pressure-retarded osmosis for power generation from salinity gradients: is it viable?, Energy Environ. Sci., 9 (2016) 31-48.

[26] S. Lin, A.P. Straub, M. Elimelech, Thermodynamic limits of extractable energy by pressure retarded osmosis, Energy Environ. Sci., 7 (2014) 2706-2714.

[27] N. Bajraktari, C. Hélix-Nielsen, H.T. Madsen, Pressure retarded osmosis from hypersaline sources—A review, Desalination, 413 (2017) 65-85.

[28] Y.C. Kim, M. Elimelech, Adverse impact of feed channel spacers on the performance of pressure retarded osmosis, J. Environ. Sci. Technol., 46 (2012) 4673-4681.

[29] D.D. Anastasio, J.T. Arena, E.A. Cole, J.R. McCutcheon, Impact of temperature on power density in closed-loop pressure retarded osmosis for grid storage, J. Membr. Sci., 479 (2015) 240-245.

[30] Q. She, X. Jin, C.Y. Tang, Osmotic power production from salinity gradient resource by pressure retarded osmosis: effects of operating conditions and reverse solute diffusion, J. Membr. Sci., 401 (2012) 262-273.

[31] K.K. Reimund, J.R. McCutcheon, A.D. Wilson, Thermodynamic analysis of energy density in pressure retarded osmosis: The impact of solution volumes and costs, J. Membr. Sci., 487 (2015) 240-248.

[32] C.F. Wan, T.-S. Chung, Osmotic power generation by pressure retarded osmosis using seawater brine as the draw solution and wastewater retentate as the feed, J. Membr. Sci., 479 (2015) 148-158.

[33] Y.C. Kim, M. Elimelech, Potential of osmotic power generation by pressure retarded osmosis using seawater as feed solution: Analysis and experiments, J. Membr. Sci., 429 (2013) 330-337.

[34] A. Achilli, T.Y. Cath, A.E. Childress, Power generation with pressure retarded osmosis: An experimental and theoretical investigation, J. Membr. Sci., 343 (2009) 42-52.

[35] N.Y. Yip, A. Tiraferri, W.A. Phillip, J.D. Schiffrnan, L.A. Hoover, Y.C. Kim, M. Elimelech, Thin-Film Composite Pressure Retarded Osmosis Membranes for Sustainable Power Generation from Salinity Gradients, J. Environ. Sci. Technol., 45 (2011) 4360-4369.

[36] M.F. Naguib, J. Maisonneuve, C.B. Laflamme, P. Pillay, Modeling pressure-retarded osmotic power in commercial length membranes, Renew Energ, 76 (2015) 619-627.

[37] J. Maisonneuve, P. Pillay, C.B. Laflamme, Pressure-retarded osmotic power system model considering non-ideal effects, Renew Energ, 75 (2015) 416-424.

[38] W. He, Y. Wang, M.H. Shaheed, Modelling of osmotic energy from natural salt gradients due to pressure retarded osmosis: Effects of detrimental factors and flow schemes, J. Membr. Sci., 471 (2014) 247-257.

[39] A.P. Straub, S. Lin, M. Elimelech, Module-scale analysis of pressure retarded osmosis: performance limitations and implications for full-scale operation, J. Environ. Sci. Technol., 48 (2014) 12435-12444.

[40] A. Altaee, A. Sharif, G. Zaragoza, N. Hilal, Dual stage PRO process for power generation from different feed resources, Desalination, 352 (2014) 118-127.

[41] A. Altaee, N. Hilal, Design optimization of high performance dual stage pressure retarded osmosis, Desalination, 355 (2015) 217-224.

[42] W. He, Y. Wang, M.H. Shaheed, Enhanced energy generation and membrane performance by two-stage pressure retarded osmosis (PRO), Desalination, 359 (2015) 186-199.

[43] A. Altaee, G. Zaragoza, E. Drioli, J. Zhou, Evaluation the potential and energy efficiency of dual stage pressure retarded osmosis process, Appl Energ, 199 (2017) 359-369.

[44] D. Bharadwaj, T.M. Fyles, H. Struchtrup, Multistage Pressure-Retarded Osmosis, J. Non-Equilib. Thermody., 41 (2016) 327-347.

[45] W. He, Y. Wang, M.H. Shaheed, Energy and thermodynamic analysis of power generation using a natural salinity gradient based pressure retarded osmosis process, Desalination, 350 (2014) 86-94.

[46] L.D. Banchik, M.H. Sharqawy, J.H. Lienhard, Limits of power production due to finite membrane area in pressure retarded osmosis, J. Membr. Sci., 468 (2014) 81-89.

[47] J.M. Prausnitz, R.N. Lichtenthaler, E.G. de Azevedo, Molecular thermodynamics of fluid-phase equilibria, Prentice-Hall, New York, 1998.

[48] M.A. Selam, Modeling Electrolyte Solutions in a Statistical Associating Fluid Theory (SAFT) Framework, in: Chemical Engineering Program, Texas A&M University, Doha, Qatar, 2017.

[49] J.A. Myers, S.I. Sandler, R.H. Wood, An Equation of State for Electrolyte Solutions Covering Wide Ranges of Temperature, Pressure, and Composition, Ind. Eng. Chem. Res., 41 (2002) 3282-3297.

[50] C. Held, L.F. Cameretti, G. Sadowski, Modeling aqueous electrolyte solutions: Part 1. Fully dissociated electrolytes, Fluid Phase Equilib., 270 (2008) 87-96.

[51] A. Zuber, R.F. Checoni, R. Mathew, J.P.L. Santos, F.W. Tavares, M. Castier, Thermodynamic Properties of 1:1 Salt Aqueous Solutions with the Electrolattice Equation of State, Oil Gas Sci. Technol., 68 (2013) 255-270.

[52] A. Zuber, R.F. Checoni, M. Castier, Thermodynamic properties of aqueous solutions of single and multiple salts using the Q-electrolattice equation of state, Fluid Phase Equilib., 362 (2014) 268-280.

[53] M.A. Selam, I.G. Economou, M. Castier, A thermodynamic model for strong aqueous electrolytes based on the eSAFT-VR Mie equation of state, Fluid Phase Equilib., 464 (2018) 47-63.

[54] B. Maribo-Mogensen, K. Thomsen, G.M. Kontogeorgis, An electrolyte CPA equation of state for mixed solvent electrolytes, AIChE J, 61 (2015) 2933-2950.

[55] D.K. Eriksen, G. Lazarou, A. Galindo, G. Jackson, C.S. Adjiman, A.J. Haslam, Development of intermolecular potential models for electrolyte solutions using an electrolyte SAFT-VR Mie equation of state, Mol Phys, 114 (2016) 2724-2749.

[56] K.S. Pitzer, Thermodynamics of Electrolytes .1. Theoretical Basis and General Equations, J. Phys. Chem., 77 (1973) 268-277.

[57] K.S. Pitzer, G. Mayorga, Thermodynamics of Electrolytes .2. Activity and Osmotic Coefficients for Strong Electrolytes with One or Both Ions Univalent, J. Phys. Chem., 77 (1973) 2300-2308.

[58] C.C. Chen, Y.H. Song, Extension of nonrandom two-liquid segment activity coefficient model for electrolytes, Ind. Eng. Chem. Res., 44 (2005) 8909-8921.

[59] S. Mattedi, F.W. Tavares, M. Castier, Group contribution equation of state based on the lattice fluid theory: Alkane–alkanol systems1, Fluid Phase Equilib., 142 (1998) 33-54.

[60] T. Lafitte, A. Apostolakou, C. Avendaño, A. Galindo, C.S. Adjiman, E.A. Müller, G. Jackson, Accurate statistical associating fluid theory for chain molecules formed from Mie segments, The Journal of chemical physics, 139 (2013) 154504.

[61] R.W. Baker, Membrane Transport Theory, Membrane Technology and Applications, (2004).

[62] W.A. Phillip, J.S. Yong, M. Elimelech, Reverse draw solute permeation in forward osmosis: modeling and experiments, J. Environ. Sci. Technol., 44 (2010) 5170-5176.

[63] N.Y. Yip, A. Tiraferri, W.A. Phillip, J.D. Schiffman, M. Elimelech, High Performance Thin-Film Composite Forward Osmosis Membrane, J. Environ. Sci. Technol., 44 (2010) 3812-3818.

[64] C.G. Broyden, A class of methods for solving nonlinear simultaneous equations, Mathematics of computation, 19 (1965) 577-593.

[65] J.H. Wegstein, Accelerating convergence of iterative processes, Commun Acm, 1 (1958) 9-13.

[66] J.P. MacHarg, G. Pique, How to design and operate SWRO systems built around a new pressure exchanger device, in: International Desalination Association World Congress Manama, Bahrain, 2002.

[67] F.-B.-A. Rahman, Modeling of Pressure Retarded Osmosis Using the Q-Electrolattice Equation of State, in: Chemical Engineering Program, Texas A&M University, Doha, Qatar, 2017.

[68] J.A. Nelder, R. Mead, A simplex method for function minimization, The computer journal, 7 (1965) 308-313.

[69] N. Saha, R. Al-Muhannadi, A. Al-Mohannadi, L.N. Véchot, M. Castier, Is it the time to say bye to the-factor?, (2017).

[70] E.W. Washburn, International Critical Tables of Numerical Data, Physics, Chemistry and Technology (1st Electronic Edition), in, Knovel.

[71] V.M. Lobo, J. Quaresma, Handbook of electrolyte solutions, Elsevier, Amsterdam, 1989.

[72] R. Stokes, A thermodynamic study of bivalent metal halides in aqueous solution. Part XVII—Revision of data for all 2: 1 and 1: 2 electrolytes at 25, and discussion of results, Trans. Faraday Soc., 44 (1948) 295-307.

[73] R.A. Robinson, R.H. Stokes, Tables of osmotic and activity coefficients of electrolytes in aqueous solution at 25 C, Trans. Faraday Soc., 45 (1949) 612-624.

[74] A.P. Straub, N.Y. Yip, M. Elimelech, Raising the Bar: Increased Hydraulic Pressure Allows Unprecedented High Power Densities in Pressure-Retarded Osmosis, Environ Sci Tech Let, 1 (2014) 55-59.

[75] W. He, Y. Wang, I.M. Mujtaba, M.H. Shaheed, An evaluation of membrane properties and process characteristics of a scaled-up pressure retarded osmosis (PRO) process, Desalination, 378 (2016) 1-13.

[76] PX Pressure exchanger, http://www.energyrecovery.com/water/px-pressure-exchanger/, 2018, (accessed 13 november 2018).

APPENDIX A

Using the definition of osmotic pressure we know that at equilibrium:

$$f_s^{\,I} = f_s^{\,II} \tag{A.1}$$

where $f_s^{\,I}$ and $f_s^{\,II}$ are the fugacities of the solvent in the solution and of the pure solvent at the same temperature, respectively. Expanding equation (A.1) and writing it in terms of its variables, we obtain:

$$x_s^I \varphi^I_{s,(T_s,P_s^I,x_s^I)} P_s^I = x_s^{II} \varphi^{II}_{s,(T_s,P_s^{II},x_s^{II})} P_s^{II} \tag{A.2}$$

where φ_s^I and φ_s^{II} are the fugacity coefficients of the solvent in the solution and of the pure solvent, respectively; x_s^I and x_s^{II} are the mole fraction of the solvent in the solution and in the pure solvent. P_s^I and P_s^{II} are the pressure of the solution and the solvent, respectively. The pressure of a pure solvent (P_s^{II}) is chosen to be at 1 atm.

To solve for P_s^I , initial guess is generated by:

$$P_s^I = -\frac{RT}{V_m^I} \ln\left(\frac{x_s \varphi_s^{\,I}(T, P_{ref}, x)}{\varphi_s^{\,II}(T, P_{ref})} \right) \tag{A.3}$$

where the fugacity coefficients are calculated using a reference pressure, P_{ref} of 1 atm and the temperature of the solution. Now assuming $\varphi_s^I \propto P_s^I$ over small intervals of P_s^I , this results in:

$$\varphi_s^I = KP_s^I + C \tag{A.4}$$

Where K is the gradient of the straight line and C is the y-intercept based on the assumption made. Substituting equation (A.4) into (A.2) and simplifying the equation and using x_s^{II} is equal to 1 for pure solvent, results in:

$$x_s^I K(P_s^I)^2 + x_s^I C(P_s^I) - \varphi_s^{II} P_s^{II} = 0 \tag{A.5}$$

Equation (A.5) can be solved using the quadratic formula. Hence for every P_k^I iteration, K_k and C_k are evaluated numerically. If the error criterion given by equation (A.6) is not satisfied, then equation (A.7) is used to provide the next guess for P_{k+1}^I

$$\frac{\left|P_k^I - P_{k-1}^I\right|}{P_k^I} \leq \varepsilon \tag{A.6}$$

$$P_{s,k+1}^I = \frac{-x_s^I C_k + \sqrt{\left(x_s^I C_k\right)^2 + 4x_s^I K_k \varphi_s^{II} P_s^{II}}}{2x_s^I K_k} \tag{A.7}$$